APPENDIX A

Principles of Similitude Applied to Scale Testing

A.1 BACKGROUND

The use of reduced-scale models to simulate the behavior of full-scale prototypes is necessary when physical testing constraints limit the feasibility of full-scale prototype testing. To achieve accurate correlation between scaled model and prototype behavior, the basic principles of similitude must be satisfied. To gain a better understanding of proper scaled modeling techniques, similitude theory and practical scale modeling for structural applications were reviewed.

Scale modeling techniques for the 1:3-scale frame test and the 1:6-scale frame tests were adapted from a 1:5-scale shaking table experiment conducted by Batt and Gavin (1999). The report of the study outlined the method for designing a 1:5-scale structural model and a method for properly scaling ground motions using similitude principles so that the proper response could be observed in the model domain. Because of the similarity of shaking table equipment and geometry to the 1:6-scale shaking table experiment described in Chapters 4 and 5, the method for developing scaling factors discussed in Batt and Gavin (1999) was ideal for developing the scaling factors for shaking table experiments of this study.

A.2 1:6 SCALING FACTOR DEVELOPMENT

The shaking table experiment was conducted at 1:5.78 of the full-scale prototype. In other words, the length scale factor, λ_L, was equal to 5.78. Other properties of the scaled experiment needed to be established to satisfy similitude principles outlined in Gavin (2003). The following development of scaling factors is adapted directly from Batt and Gavin (1999).

Strain (ε) was chosen as the dimensionless property that would be preserved between the full-scale prototype and the scale model:

$$\varepsilon_m = \varepsilon_p \tag{A-1}$$

where "m" and "p" designate model and prototype properties respectively. Using Hooke's Law:

$$E = \frac{\sigma}{\varepsilon} \tag{A-2}$$

where E is the modulus of elasticity and σ is normal stress, the following relationship can be obtained:

$$\frac{\sigma_m}{E_m} = \frac{\sigma_p}{E_p} \tag{A-3}$$

Because steel was used for the prototype and the scale model, it is observed that:

$$E_m = E_p = \text{Young's Modulus} \tag{A-4}$$

and therefore:

$$\sigma_m = \sigma_p \tag{A-5}$$

Since stress can be expressed in terms of force (F) and length (L):

$$\sigma = \frac{F}{L^2} \tag{A-6}$$

it follows that:

$$\frac{F_m}{L_m^2} = \frac{F_p}{L_p^2} \tag{A-7}$$

Substituting Newton's Second Law:

$$F = MA = \frac{ML}{T^2} \tag{A-8}$$

where M is mass and T is time, and A is gravitational acceleration, the following equation can be obtained:

$$\frac{M_m}{L_m T_m{}^2} = \frac{M_p}{L_p T_p{}^2} \tag{A-9}$$

or

$$\frac{M_p}{M_m} = \frac{L_p T_p{}^2}{L_m T_m{}^2} \tag{A-9}$$

This can be expressed in terms of scaling factors (λ) for mass, length, and time, which are ratios of the model-scale value divided by the full-scale prototype value:

$$\lambda_M = \lambda_L \lambda_T^2 \tag{A-10}$$

Acceleration was also chosen to be preserved between the scale model and the prototype:

$$\lambda_A = 1 \tag{A-11}$$

The acceleration factor can also be expressed in terms of length and time:

$$\lambda_A = \frac{\lambda_L}{\lambda_T^2} = 1 \tag{A-12}$$

The time scale factor can then be expressed in terms of the length scale factor:

$$\lambda_T = \sqrt{\lambda_L} \tag{A-13}$$

Based on the length scale factor (λ_L=5.78), mass and time scaling factors required are set as follows:

$$\lambda_T = \sqrt{\lambda_L} = \sqrt{5.78} = 2.404 \tag{A-14}$$

$$\lambda_M = \lambda_L \lambda_T^2 = (5.78)(2.404)^2 = 33.4 \tag{A-15}$$

APPENDIX B

Shaking Table Description and Capacity Verification Tests

B.1 SHAKING TABLE DESCRIPTION

The uni-directional, small-scale shaking table (Figures B.1 and B.2), located in the Interdisciplinary Materials Research Servo-hydraulic Testing Laboratory (107 Hancock Hall), is composed of a 5 ft x 5 ft x 3 in. aluminum table, which translates in one direction on a roller-bearing / rail system. One-half inch diameter holes are tapped in the table on a 6 in. grid, with the greatest spacing between the holes equaling 4ft 6in. in both directions. The table is moved by a 3000 psi MTS servo-hydraulic system including a dynamic actuator, servo-valve, and service manifold. The MTS actuator (model no. 244.22) has a force capacity equal to 22,000 lb and a 6.0-in dynamic stroke. The MTS servo-valve (model no. 252.32) has a maximum flow-rate equal to 60 gallons per minute (gpm). The MTS service manifold (model no. 290.14) houses two 475 cc and one 975 cc MTS accumulators. The servo-hydraulic system is powered by a 70 gpm capacity pump, which services several machines in the laboratory simultaneously. Control over the system is provided by a 5150 Series Schenck-Pegasus controller (Figure B.3) which operates based on position feedback from a linear voltage displacement transducer (LVDT), housed in the MTS actuator.

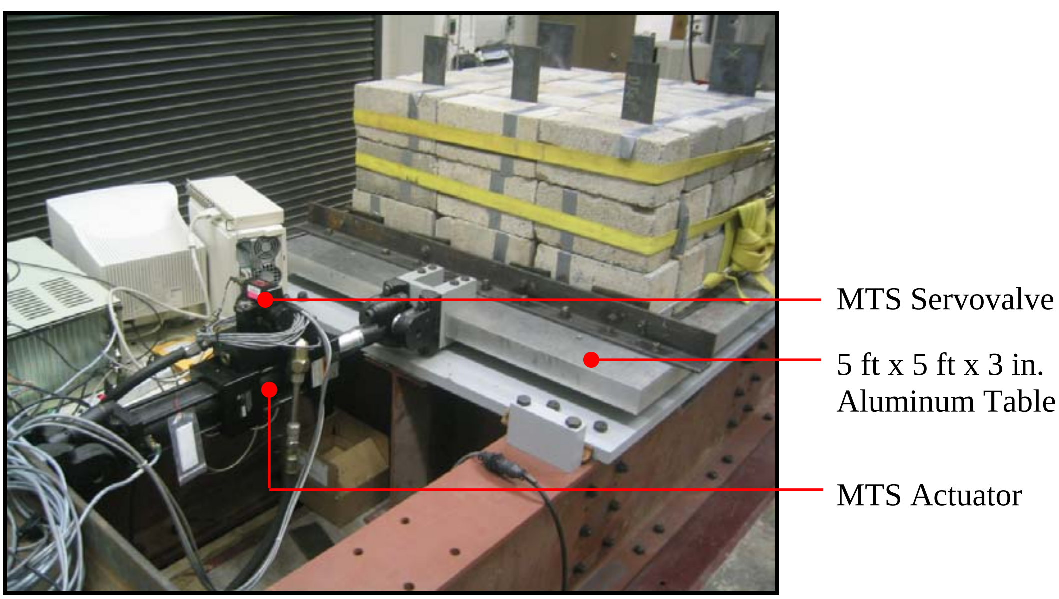

Figure B.1: Overview Photo of Shaking Table with Test Ballast in Place

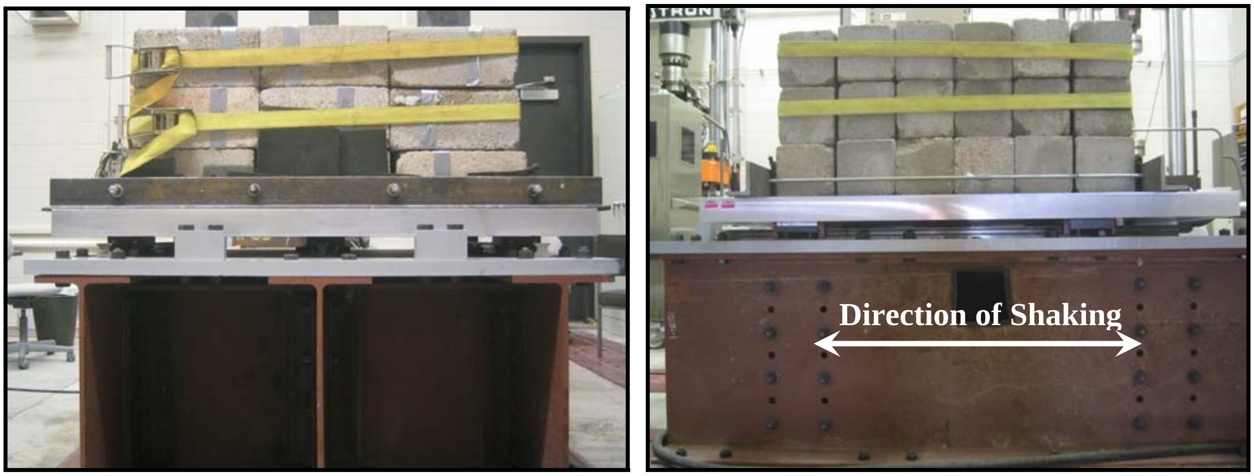

a) East Side View **b) North Side View**

Figure B.2: Side View Photos of Shaking Table with Test Ballast in Place

Figure B.3: Photo of 5910 Schenck-Pegasus Controller

B.2 SHAKING TABLE CAPACITY VALIDATION TESTING

B.2.1 OVERVIEW

To determine the mass limit of the scale frame which could be excited with the appropriate scaled ground motion by the shaking table system, ballast tests were conducted. The tests consisted of incrementally adding ballast composed of solid concrete blocks to the table and exciting the table with scaled Northridge ground-motion history. The intensity of the scaled ground motion history was also increased incrementally at each ballast load level. Table B.1 summarizes all test cases. For each test the input displacement signal, MTS internal LVTD measured displacement and table acceleration were recording in real time at a 0.0195 sec interval. The recorded values were adjusted to the full-scale using scaling factors for displacement (λ_L) and time (λ_T) and compared to the prototype acceleration in the time and frequency domains.

Table B.1: Test Case Summary

Test ID	Ballast Weight (lb)	Percentage of Scaled Ground Motion	Bandwidth (Hz)	Record Length (sec)	Time Domain Resolution (sec)	Frequency Domain Resolution (Hz)
101305-1	Table Only	100 %	20	160	0.0195	0.0063
101305-1	1,470	100%	20	160	0.0195	0.0063
101305-2	1,470	120%	20	160	0.0195	0.0063
101305-3	1,470	140%	20	160	0.0195	0.0063
101705-1	2,630	100%	20	160	0.0195	0.0063
101705-2	2,630	120%	20	160	0.0195	0.0063
101705-3	2,630	140%	20	160	0.0195	0.0063
101705-4	3,700	100%	20	40	0.0195	0.025
101705-5	3,700	120%	20	40	0.0195	0.025
101705-6	3,700	140%	20	40	0.0195	0.025
101705-1	4,750	120%	20	40	0.0195	0.025
101705-2	4,750	168%	20	40	0.0195	0.025
101705-3	4,750	198%	20	40	0.0195	0.025

B.2.2 GROUND MOTION INPUT

The Northridge ground motion chosen for the scale frame shaking table experiment was also used for the capacity validation testing. Since the table is controlled based on position feedback from a linear voltage displacement transducer (LVDT), a voltage function, representing the desired table position in time, was required to control the table. To replicate the acceleration history of the Northridge event at the 1:5.78 scale with a nearly continuous voltage function, the following steps were followed:

Step 1: The Northridge displacement history, which consisted of a table of ground displacement values recorded at a constant 0.02 second increment, were procured.

Step 2: The displacement history was converted to the 1:5.78 scale by dividing the table of displacements by the length scale factor (λ_L), and dividing the time increment by the time scale factor (λ_T).

Step 3: Scaled displacement table was converted to a representative voltage table, based on the sensitivity of the LVDT in which ±10 volts equals ±3 in.

Step 4: A table of voltages and change of voltage rates was created, based on two point linear interpolation between consecutive voltage values.

The resulting tables of voltages and rates were combined to create a nearly continuous voltage function which was read into Schenck-Pegasus controller as an external position control signal. An example of the signal compared with the actual position reported by the LVDT is shown in Figure B.4. Both signals are plotted as displacements. It should be noted that, while a slight time lag exists between the input signal and LVDT output signal, the values of the displacement (voltage x 0.30) histories are nearly identical.

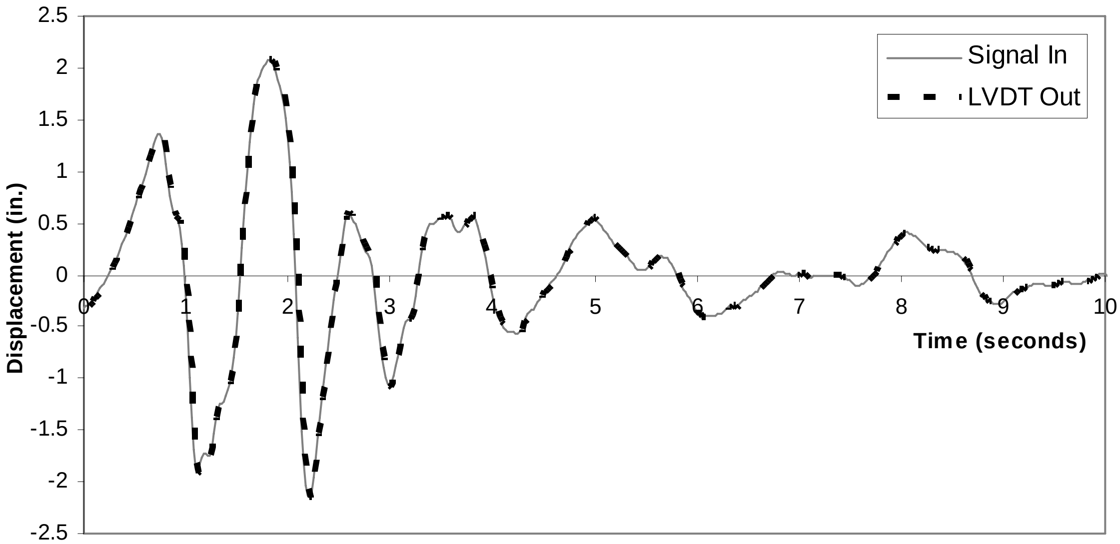

Figure B.4: Control Signal vs. LVDT Displacement

B.2.3 DATA RECORDING

Acceleration and the input displacement signal were measured for all test cases. To optimize the time and frequency domain resolution, all measurements were taken using a 20 Hz bandwidth and either a 160 second or 40 second time history length. The chosen bandwidth was based on the scaled ground motion being recorded and the resonant frequencies of the 1:5.78 scale frame. As shown in Figure B.5, the vast majority of acceleration for the scaled Northridge ground motion falls within this bandwidth. The first and second resonant frequencies (f_1 and f_2) also fall within the chosen bandwidth. It should be noted that Figure B.5 is presented in the 1:5.78 scale with respect to time.

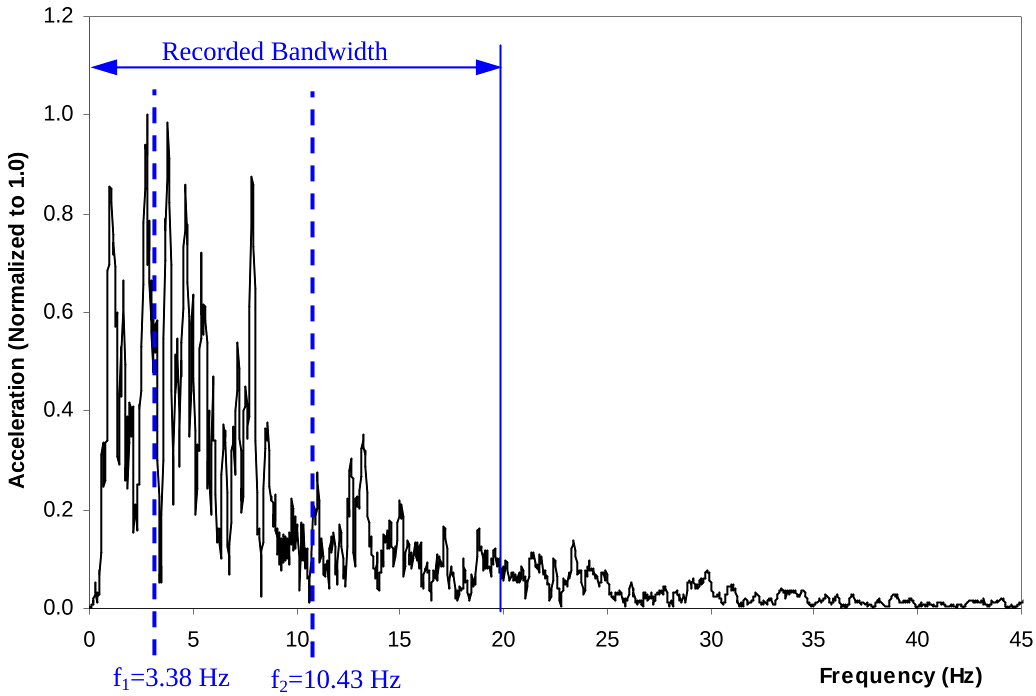

Figure B.5: FFT of 1:5.78 Scale Northridge Ground Acceleration

It was also important to verify that the data being collected was accurately correlated, and repeatable. Therefore, each test listed in Table B.1 consists of three separate loading cycles to determine the coherence function. The coherence function was used to validate the system input and output data collected to ensure that acceleration data being collected was due to the input displacement signal. The coherence function was based on the transfer function between the input displacement and acceleration for a series of three separate excitations of the shake table using identical displacement histories. The coherence function for Test 101705-2 is shown in Figure B.6. In general the coherence function is equal to 1.0 for frequencies in which a correlation between input displacement and recorded acceleration is perfectly validated. In this case, the coherence function was determined to be ideal between 0.46 Hz and 7.75 Hz, acceptable between 7.75 Hz and 13.5 Hz, and unacceptable above 13.5 Hz. It should be noted that the coherence function appears to fall apart above 13.5 Hz primarily due to a significant reduction in input signal above this frequency as shown in Figure B.5. Based on the coherence function, it was determined that acceleration data recorded between 0.46 Hz and 13.5 Hz was reliable. Since the vast majority of ground acceleration and the first two resonant frequencies occur in this range, this was determined to be acceptable.

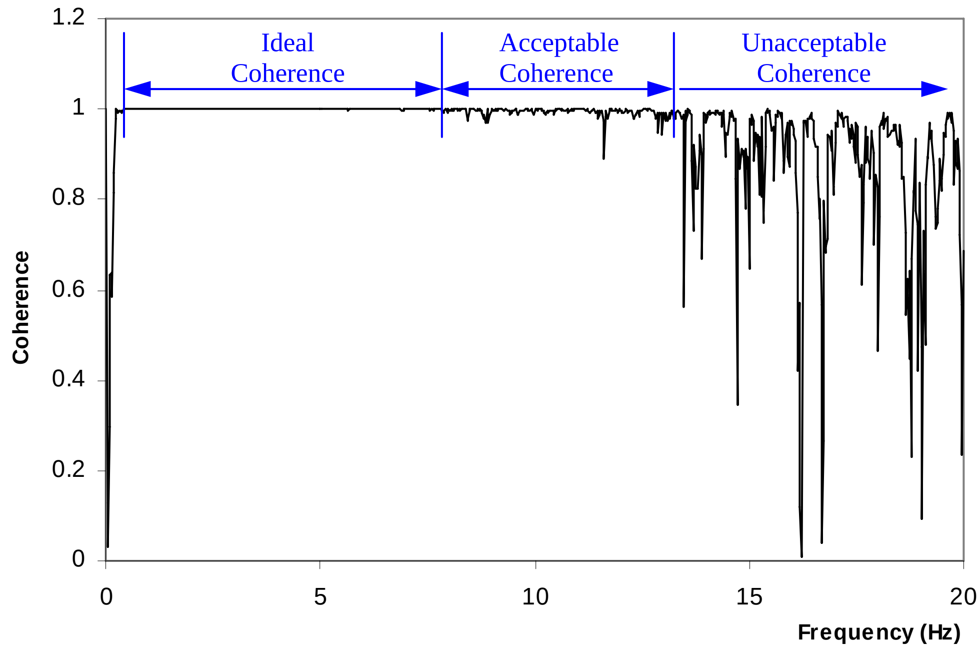

Figure B.6: Coherence Function for Test 101705-2

B.2.4 RESULTS

The goal of the shaking table capacity tests was to validate the maximum mass which could be excited by the shaking table with the appropriate ground motion. Closely matching the scaled acceleration history, while maintaining fidelity in the frequency domain, was of primary importance. Comparisons of the acceleration history of the shaking table versus the actual full-scale Northridge acceleration history of the full-scale ground motion and the acceleration autospectrum (FFT) of the shaking table versus acceleration autospectrum of the Northridge ground motion as mass and scaled ground motion intensity were increased were used to determine a reasonable mass limit. Comparisons from all tests conducted prior to Test 101705-1 appear very similar to the comparisons of Test 101705-1. Tests 101705-2 and 101705-3 varied somewhat from Test 101705-1, indicating that a mass limit at the required acceleration level was being approached. Therefore, the comparison results of the final three tests are presented and commented on herein.

For Tests 101705-1 through 101705-2, it was observed that spiking at peaks throughout the acceleration history above the desired ground motion peaks becomes more prominent as acceleration intensity increased (Figures B.7, B.9, and B.10). It was determined that the spiking was a result of the shaking table frame responding to inertial loads generated by the mass, and an indication that the mass limit that could be controlled by the shaking table system at the desired acceleration was being approached. It should be noted that all scaled acceleration histories were converted to full-scale for comparison with the Northridge acceleration history.

The fidelity in the frequency domain was also considered by comparing the autospectra of the scaled ground motion to that of the full-scale ground motion (Figures B.8, B.10, and B.12). Overall the autospectra of the scaled accelerations match those of the full-scale ground motion acceleration closely. However, the matching was observed to be progressively less precise as the intensity of the ground motion was increased. It should be noted that all scaled autospectrums were converted to full-scale for comparison with the Northridge autospectrum.

It was concluded that a mass limit equal to 0.0122 k-s^2/in. (4,700 lb) be placed on the 1:5.78 scale frame planned for the shaking table experiment.

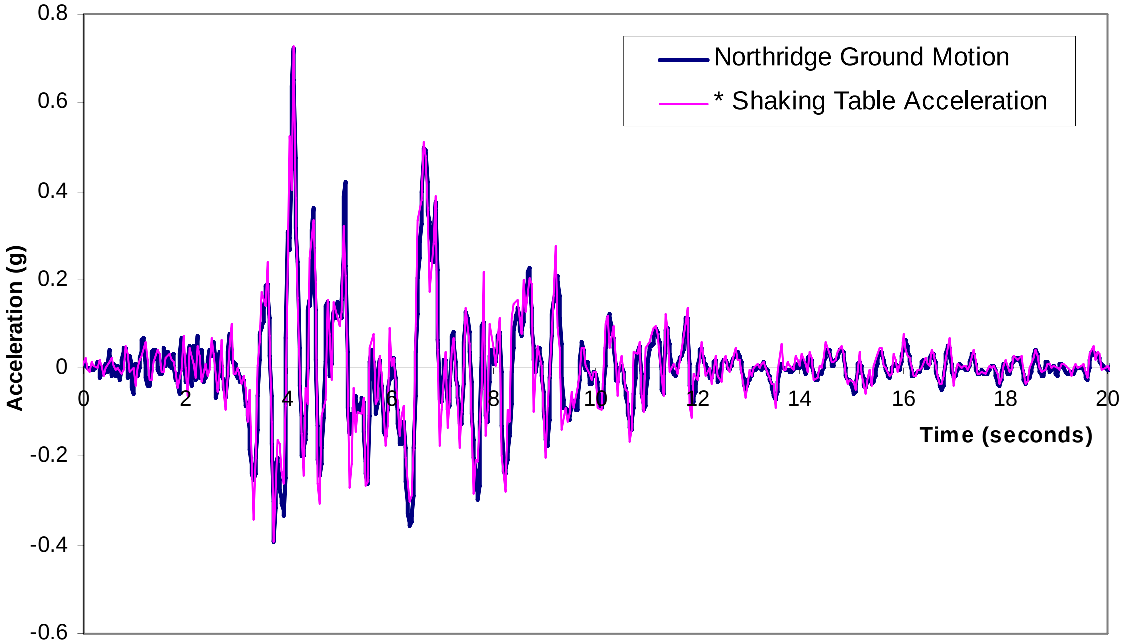

* Time multiplied by λ_T and displacement multiplied by λ_L for comparison to full scale

Figure B.7: Acceleration History Comparison: Test 101705-1

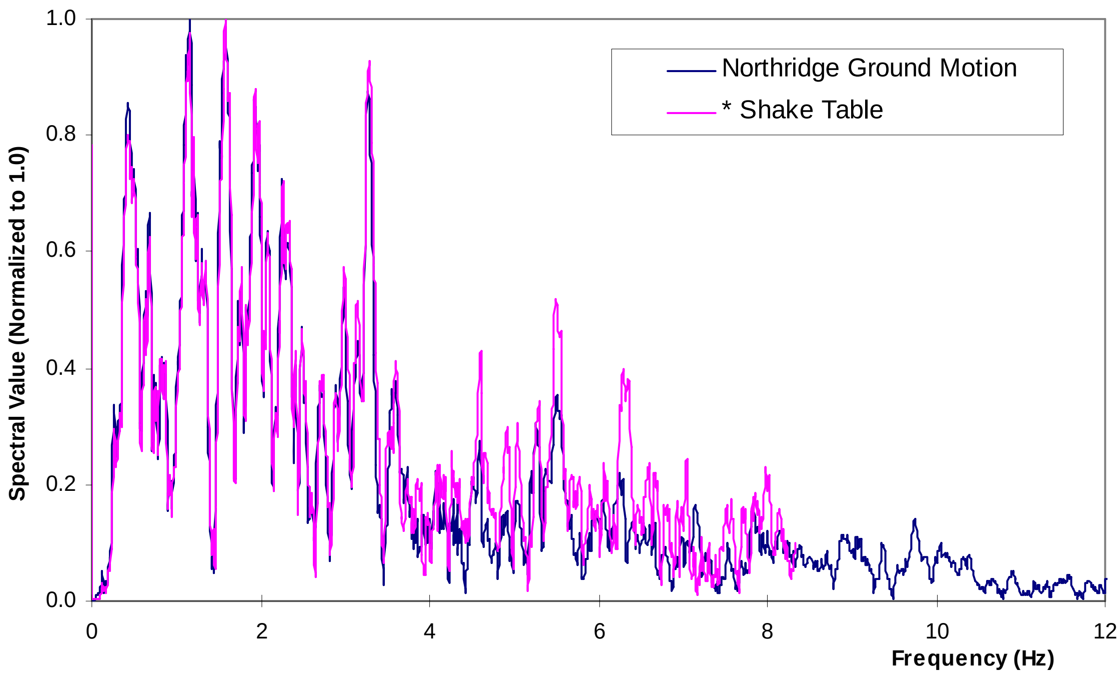

* Time multiplied by λ_T for comparison to full scale

Figure B.8: Acceleration Autospectrum Comparison: Test 101705-1

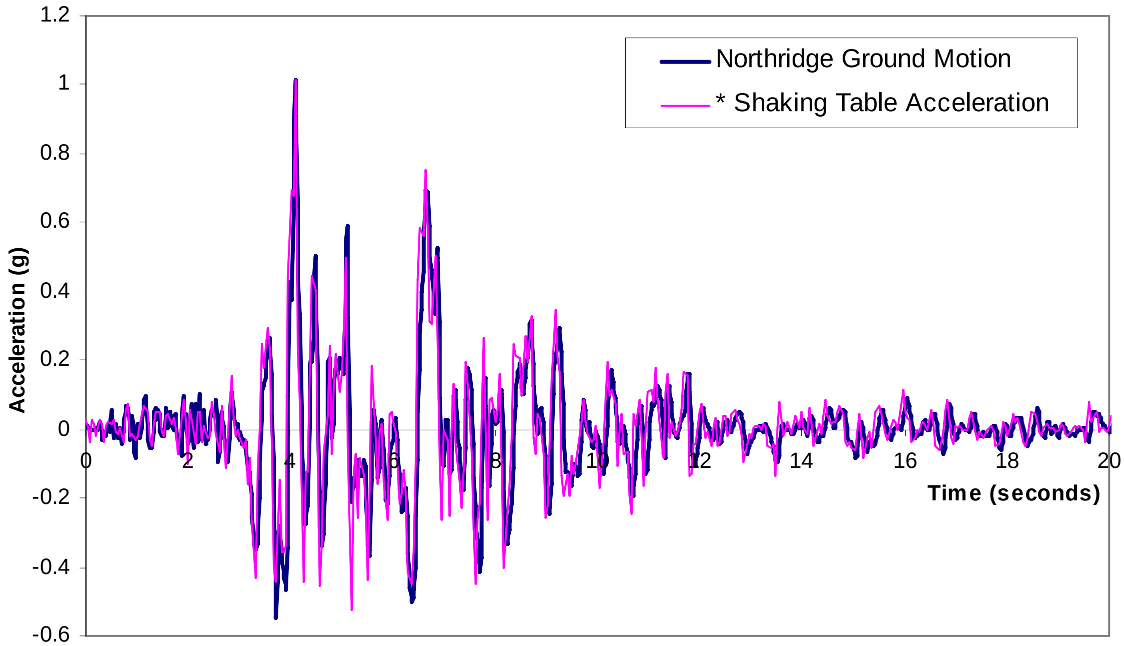

* Time multiplied by λ_T and displacement multiplied by λ_L for comparison to full scale

Figure B.9: Acceleration History Comparison: Test 101705-2

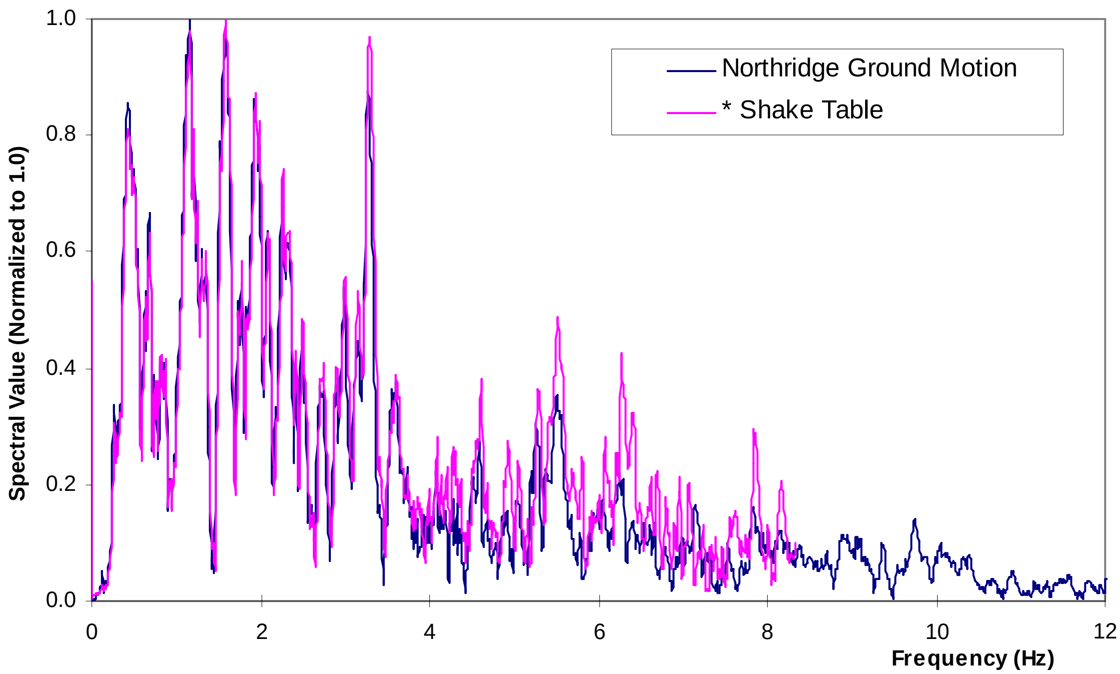

* Time multiplied by λ_T for comparison to full scale

Figure B.10: Acceleration Autospectrum Comparison: Test 101705-2

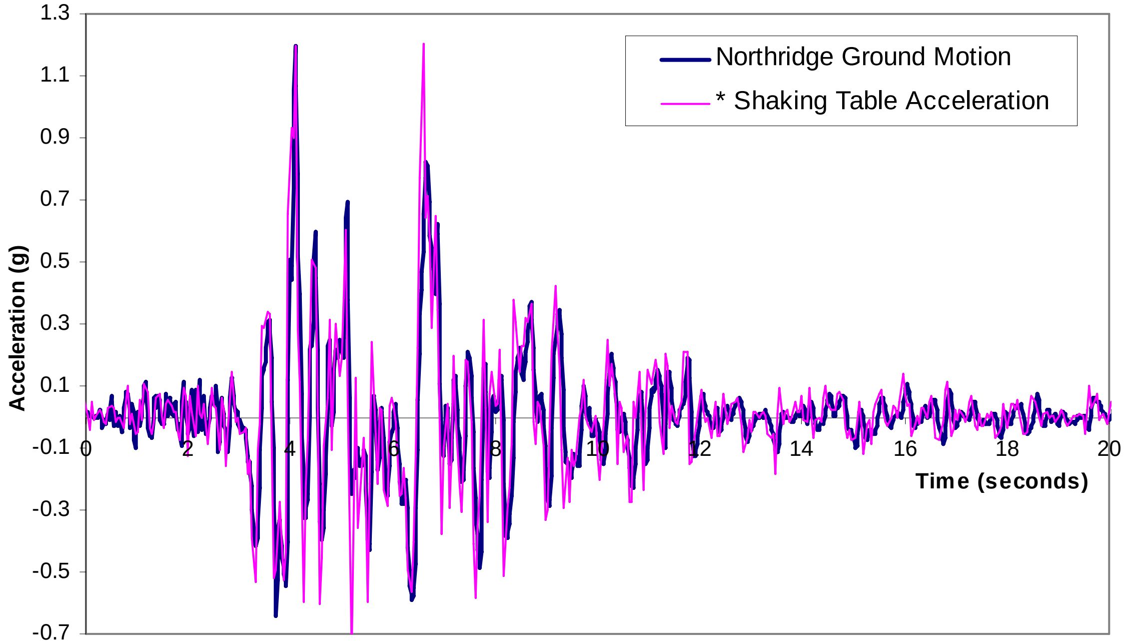

* Time multiplied by λ_T and displacement multiplied by λ_L for comparison to full scale

Figure B.11: Acceleration History Comparison: Test 101705-3

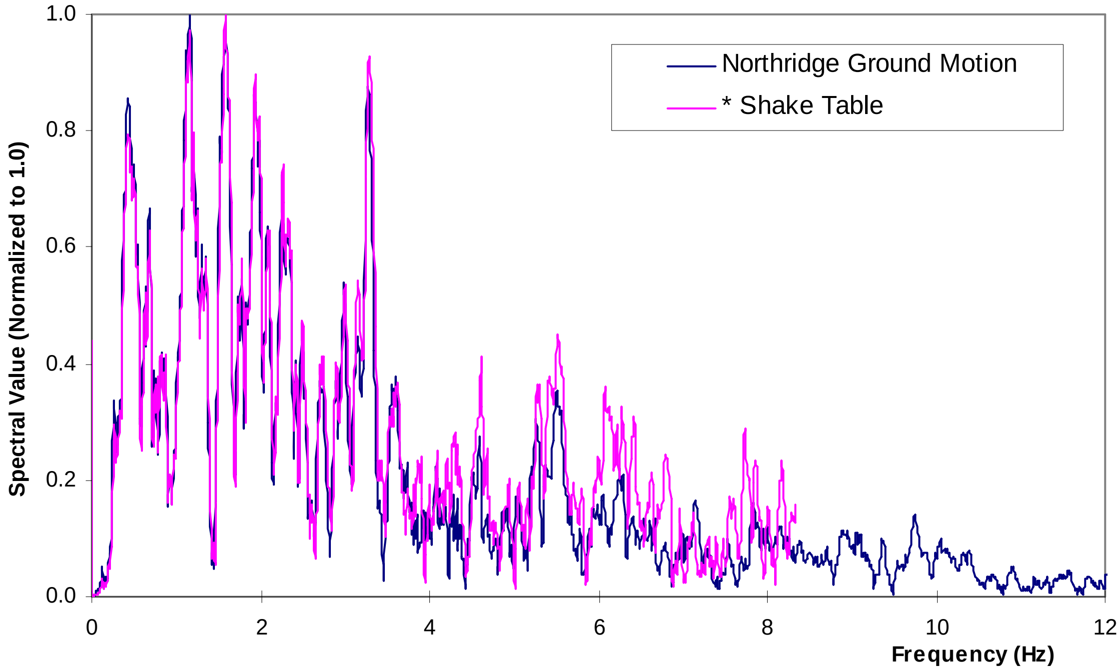

* Time multiplied by λ_T for comparison to full scale

Figure B.12: Acceleration Autospectrum Comparison: Test 101705-2

APPENDIX C

Steel Hinge Response Development Example

C.1 INTRODUCTION

A steel hinge definition was developed and implemented in DRAIN for all analyses of this study. Theoretical background for the hinge definition can be found in Charney (2006). The procedure described in Charney (2006) was adapted directly and used to define the moment-rotation response for each steel cross-section used. This Appendix generally describes the steps taken to develop hinge definitions for use in DRAIN. An example calculation is presented to illustrate the use of the steps required for the development of the hinge definition for a W18x50-A992, which was used to model the roof and floor beams of the full-scale prototype frame in Chapter 3.

C.2 GENERAL PROCEDURE

The following steps were taken to develop each plastic hinge definition:

1. Establish a bilinear stiffness material response curve for each grade of steel considered. (This included ASTM material specification A-992 for W-shapes and A-500 steel for hollow structural members for this study.)
2. Based on Step 1, develop a moment-versus-rotation response curve using the cross-sectional properties of each standard steel section used.
3. Based on hinge formation at a distance equal to one-half of the beam depth from the face of the column, and a point of inflection at the mid-point of the beam in a moment frame, develop a moment-versus-deflection response curve at the point of inflection using moment at the face of the column due to a point load at the point of inflection.
4. In DRAIN, model the beam as a cantilever with a fixed end and a point load applied at the free end, using two Type 2 elements with a common node location at the point of assumed hinging. Using the master/slave node functionality of DRAIN, create dependent translational degrees of freedom and an independent rotational degree of freedom between the end nodes of each element. Use two Type 4 elements to replicate the moment-versus-rotation response at the hinge.

5. Vary the Type 4 element definition parameters to replicate the moment-versus-rotation response curve developed in Step 3.

C.3 Example

The following steps were used to develop the plastic hinge response of the W18x50-A992 sections used in the full-scale prototype analyses of Chapter 3. All other plastic hinge definitions were developed similarly.

Material and Section Properties:

Standard AISC Section: W18x50

Member Depth (d) = 18 in.

Cross-sectional Area (A) = 14.7 in.^{2}

Moment of Inertia (I_x) = 800 in.^{4}

Flange Thickness (t_f) = 0.57 in.

Web Thickness (t_w) = 0.35 in.

ASTM Material Specification: A-992

Yield Stress (F_y) = 50 ksi

Ultimate Stress (F_u) = 65 ksi

Modulus of Elasticity (E) = 29,000 ksi

Step 1: The bilinear material response curve is shown in Figure C.1. The initial stiffness is equal to 29,000 ksi between 0 ksi and 50 ksi stress. The secondary stiffness above 50 ksi includes strain hardening expressed as a percentage of the modulus of elasticity. Three percent strain hardening was ultimately used for analyses of the full-scale prototype frame, and is therefore used for calculations presented herein. A more detailed explanation of this material response curve is provided in Charney (2006).

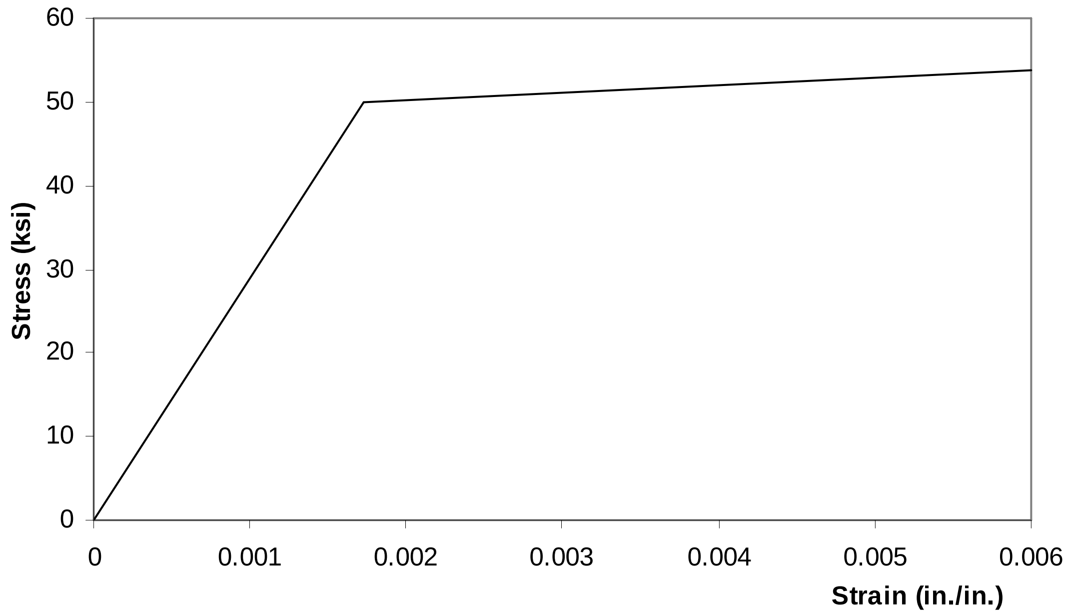

Figure C. 1: Material Response Curve: 3% Strain Hardening

Step 2: A Microsoft Excel spreadsheet was used to calculate the moment-versus-rotation response curve for the beam. The beam cross-section was broken into 25 horizontal segments above and below the neutral axis. Each flange was broken into 10 horizontal slices, and the web was broken into 15 horizontal slices between the neutral axis and the bottom of the flange. The "k"-area at the flange-to-web interface was equally distributed among the web slices. A linear relationship between curvature (ϕ) and strain was assumed. Example calculations for moment corresponding to 0.002 rad/in. and 0.005 rad/in. are shown in Table C.1. Area (A_i), distance from the neutral axis (d_i), stress corresponding to the strain at the given curvature (f_{di}), and moment contributed (M_i) for each slice of flange and web area were calculated for each rotation condition. Strain was approximated to be uniform for each portion of the flange and web, and was equal to the distance from the neutral axis to the centroid of the segment multiplied by sin(ϕ). The stress of the segment, f_{di}, was determined from the stress-strain relationship shown in Figure C.1. The moment contribution of each segment was then calculated as follows:

$$M_i = A_i f_{di} d_i \tag{C-1}$$

Summing the contribution to the moment from each side of the neutral axis resulted in one-half of the moment associated with the given rotation. Using symmetry, the full moment of the section was calculated by multiplying the sum by two. This was done for several values of ϕ, resulting in a moment-versus-rotation curve with a smooth transition through the elastic limit. The resulting moment-versus-rotation curve is shown in Figure C.2.

Table C. 1: Example Calculation of Moment Corresponding to 0.002 and 0.005 rad Rotation

				ϕ = 0.0002 rad/in.		ϕ = 0.0005 rad/in.	
		A_i (in.^{2})	d_i (in.)	f_{di} (ksi)	M_i (in-k)	f_{di} (ksi)	M_i (in-k)
Flange Contribution	F_1	0.43	8.97	50.06	192	52.28	200
	F_2	0.43	8.91	50.05	191	52.26	199
	F_3	0.43	8.86	50.04	189	52.24	198
	F_4	0.43	8.80	50.03	188	52.21	196
	F_5	0.43	8.74	50.02	187	52.19	195
	F_6	0.43	8.69	50.01	186	52.16	194
	F_7	0.43	8.63	50.00	184	52.14	192
	F_8	0.43	8.57	49.72	182	52.12	191
	F_9	0.43	8.52	49.39	180	52.09	190
	F_{10}	0.43	8.46	49.06	177	52.07	188
Web Contribution	W_1	0.21	8.15	47.26	79	51.94	87
	W_2	0.21	7.59	44.00	69	51.71	81
	W_3	0.21	7.03	40.75	59	51.48	74
	W_4	0.21	6.46	37.49	50	51.25	68
	W_5	0.21	5.90	34.23	41	51.01	62
	W_6	0.21	5.34	30.97	34	50.78	56
	W_7	0.21	4.78	27.71	27	50.55	50
	W_8	0.21	4.22	24.45	21	50.32	44
	W_9	0.21	3.65	21.19	16	50.08	38
	W_{10}	0.21	3.09	17.93	11	44.82	28
	W_{11}	0.21	2.53	14.67	8	36.67	19
	W_{12}	0.21	1.97	11.41	5	28.52	12
	W_{13}	0.21	1.41	8.15	2	20.37	6
	W_{14}	0.21	0.84	4.89	1	12.22	2
	W_{15}	0.21	0.28	1.63	0	4.07	0
	1/2	of Total	Moment:	SUM =	2278	SUM =	2567
			Total	Moment =	**4556**		**5134**

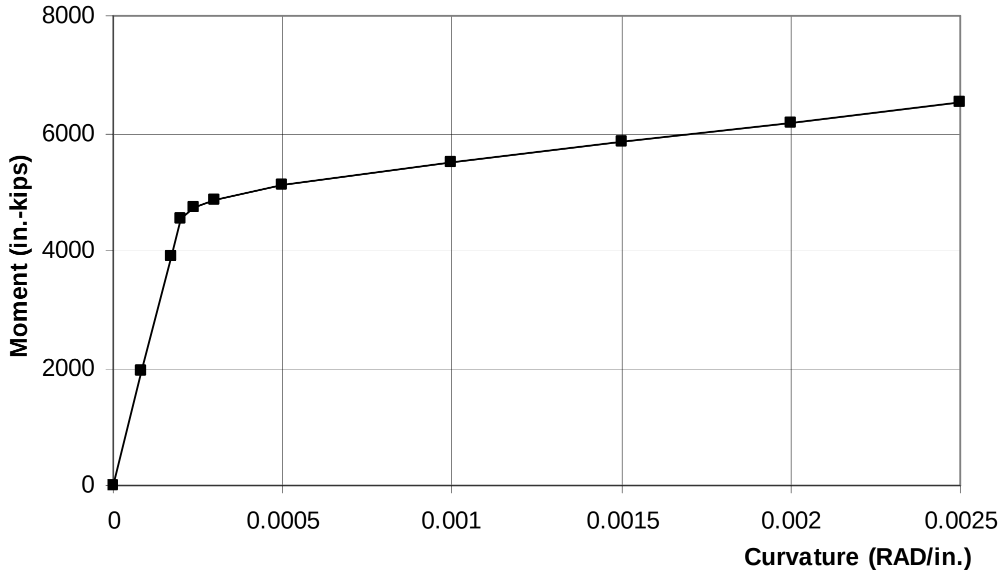

Figure C. 2: Moment-Rotation Curve: W18x50-A992

Step 3: Moment-versus-deflection was calculated based on the model in Figure C.3. The tip deflection consists of two parts: elastic deflection of the beam due to a point load, and deflection due to the rotation at the plastic hinge, based on the moment-versus-rotation response developed in Step 4. The total moment-versus-tip-deflection curve is shown in Figure C.4. Similar curves were also developed for one and five percent strain hardening and are included in Figure C.4 for comparison.

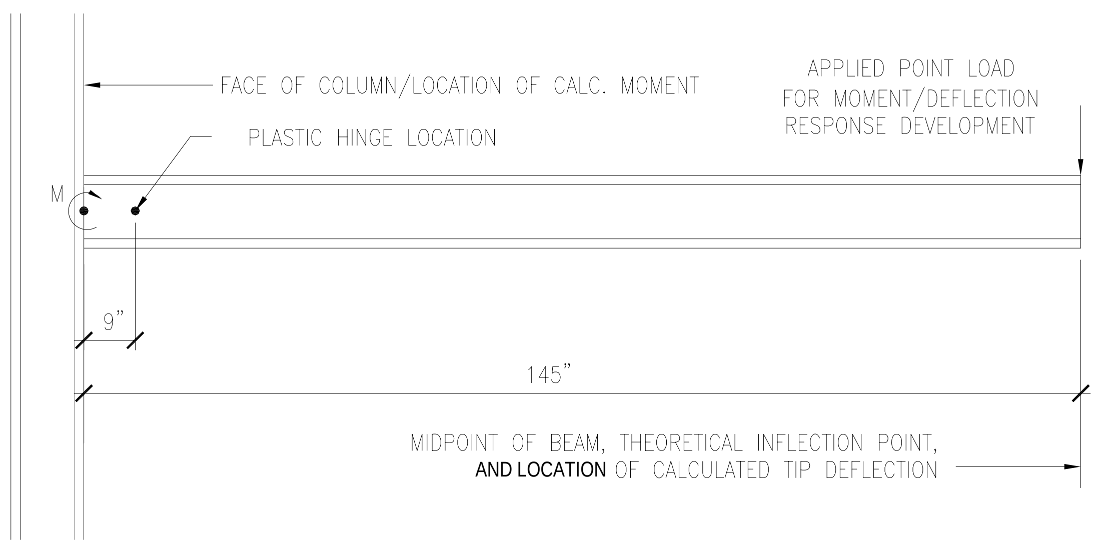

Figure C. 3: Model of Beam with Hinge

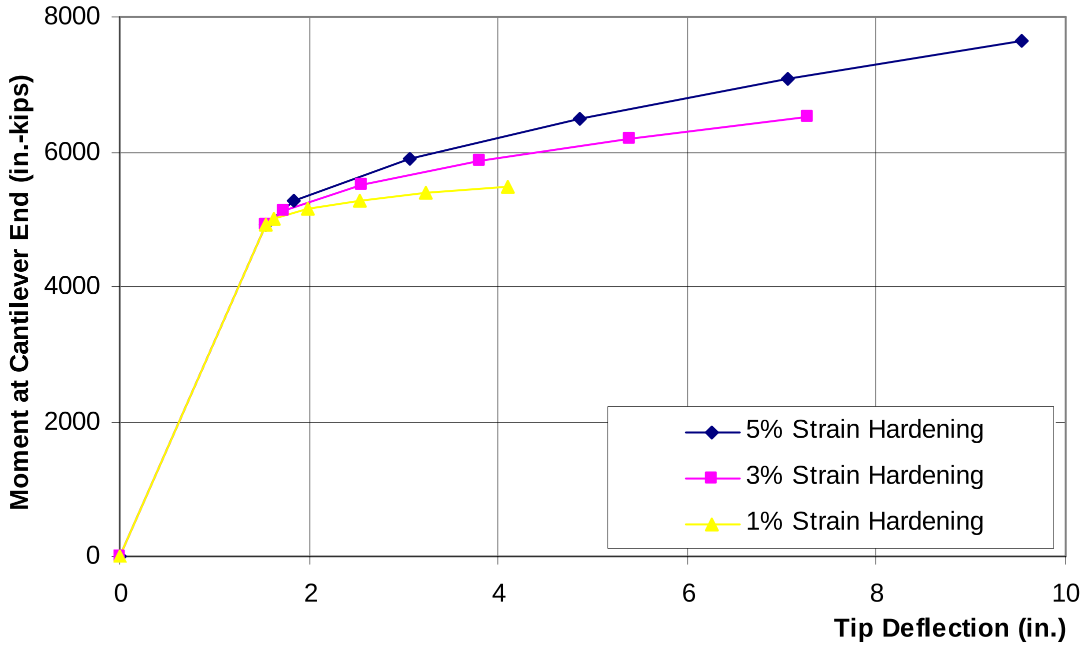

Figure C. 4: Moment Versus Tip Deflection: W18x50-A992

Step 4: The cantilever modeled in DRAIN is shown in Figure C.5. The model consists of two elastic beam elements (Type 2 Elements), defined with the material and cross-sectional properties of a standard W18x50-A992 shape. At the hinge location, two non-linear rotational spring elements (Type 4 Elements) were used. A general form of the hinge definitions is presented in Chapter 3.

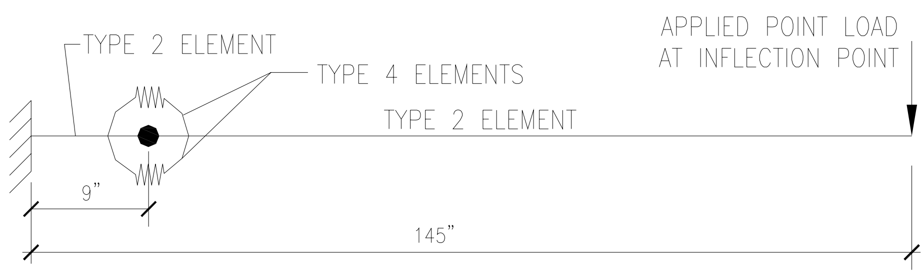

Figure C. 5: Cantilever Model in DRAIN

Step 5: To calibrate the hinge with the moment-versus-tip-deflection response found in Step 3, a point load was applied incrementally at the tip of the cantilever. The yield moment of the hinges and the initial and secondary stiffnesses were varied in DRAIN until a close match to the moment-versus-deflection response curve of Step 3 was obtained (Figure C.7). Response curves for one and five percent strain hardening are shown for comparison.

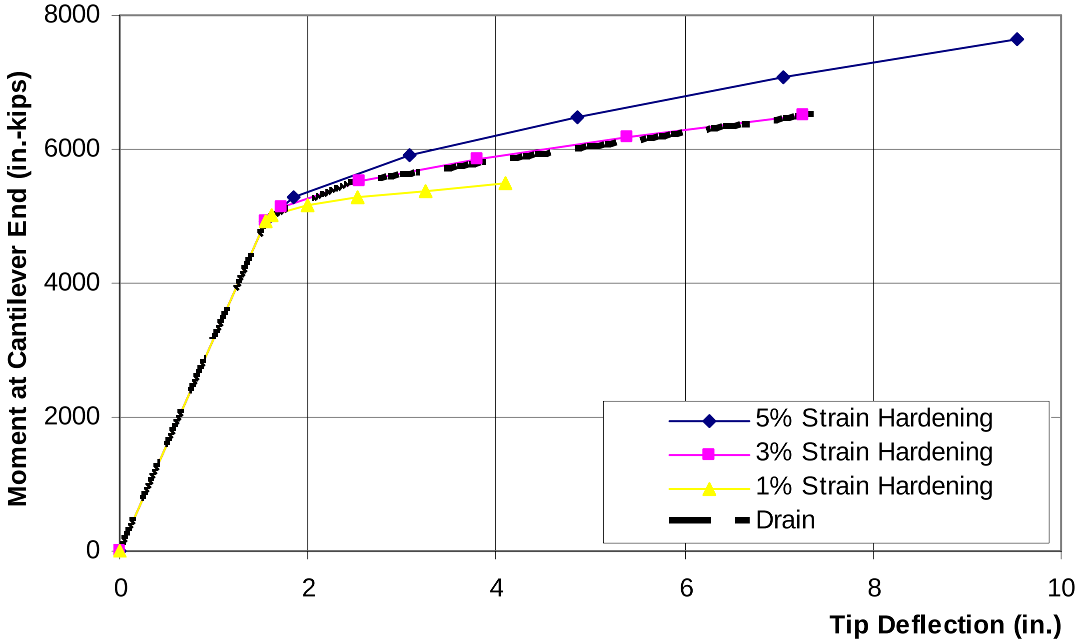

Figure C. 7: Calibration of Hinge Definition

APPENDIX D

DRAIN-2DX Study of 1:3-Scale Frame Tests

D.1 OVERVIEW

An analytical study was conducted on the 1:3-scale frame model to investigate the adequacy of the DRAIN model for predicting the response of the 1:6-scale shaking table experiment. Specifically 5 tests were simulated and are listed in Table D.1. These tests were chosen because of the large excursions observed resulting in inelastic frame behavior, and an extreme range of loading observed in the ropes. Load histories measured during each test are shown in Figure D.1, and were used for DRAIN simulations.

The general DRAIN model described in Chapter 3 was used for defining the steel frame and the ropes. A diagram of the model used for the 1:3-scale frame tests is shown in Figure D.1. Moments of inertia and cross-sectional areas of beam and column members were taken from standard tables of AISC (2005). Because the bending stiffnesses at the panel zone and connections were difficult to quantify, these values were adjusted uniformly such that the initial lateral stiffness of the frame, determined in Chapter 2, was matched in the DRAIN model. Beam and column hinges were defined using the method described in Chapter 3. Yield stress of the steel was assumed to be 50 ksi, and strain hardening was assumed to occur at 3% of Young's Modulus. Rope response definitions were based on quasi-static rope tests described in Chapter 2. Rope preload was defined using the built in pretension functionality of the Type 9 element. Loading was applied as indicated in Figure D.2. Displacements at the load point for all simulations and rope forces for Tests 27 and 29 were recorded and compared to experimental results.

Table D.1: List of Experimental Tests Modeled

Test No.	Test Group	Amp.	Freq.	PT	Load Cycles
26	I.S.-Frame-	11k -	0.75Hz		5
27	I.S.-Rope -	12k -	0.75Hz -	PTj	5
28	I.S.-Frame-	12k -	0.75Hz		5
29	I.S.-Rope -	14k -	0.75Hz -	PTk	5
36	I.S.-Frame-	14k -	0.5Hz -		5

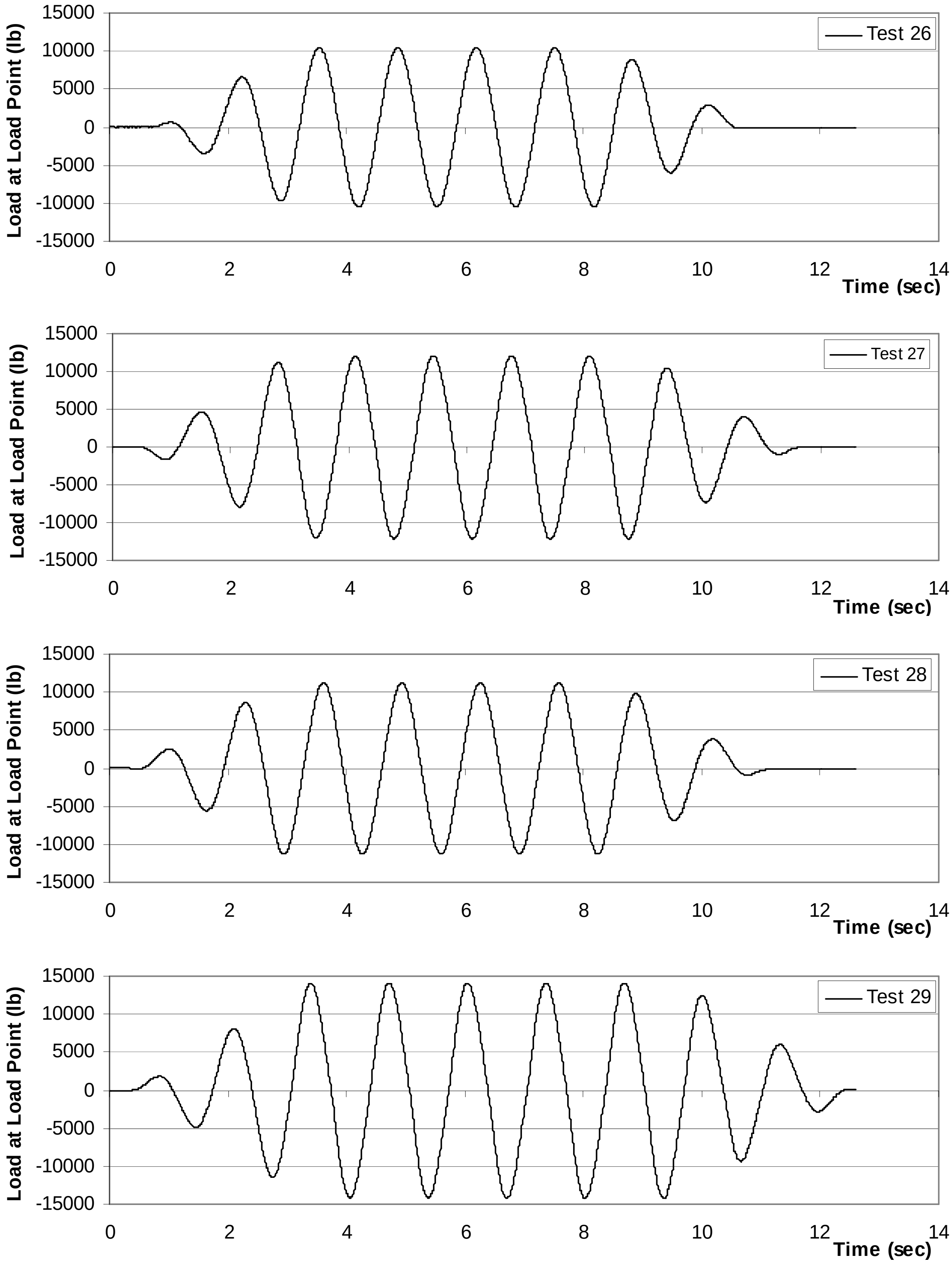

Figure D.1: Loading Histories

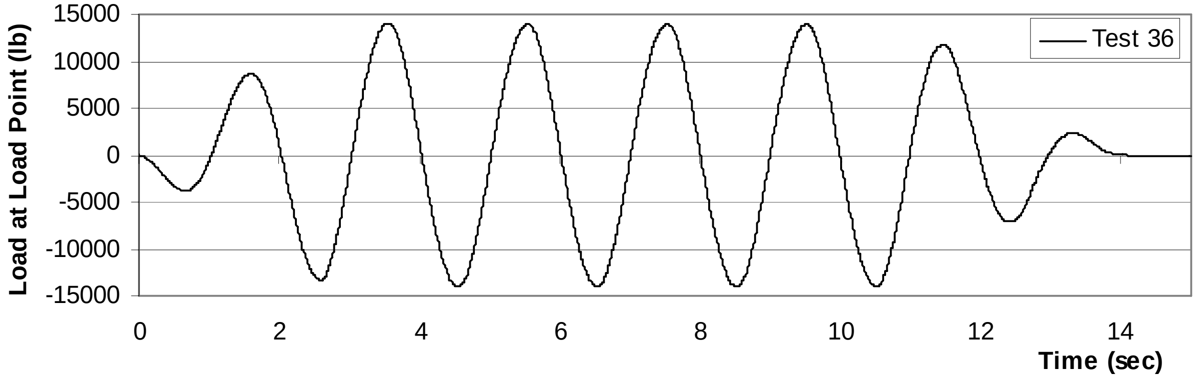

Figure D.1(Continued): Loading Histories

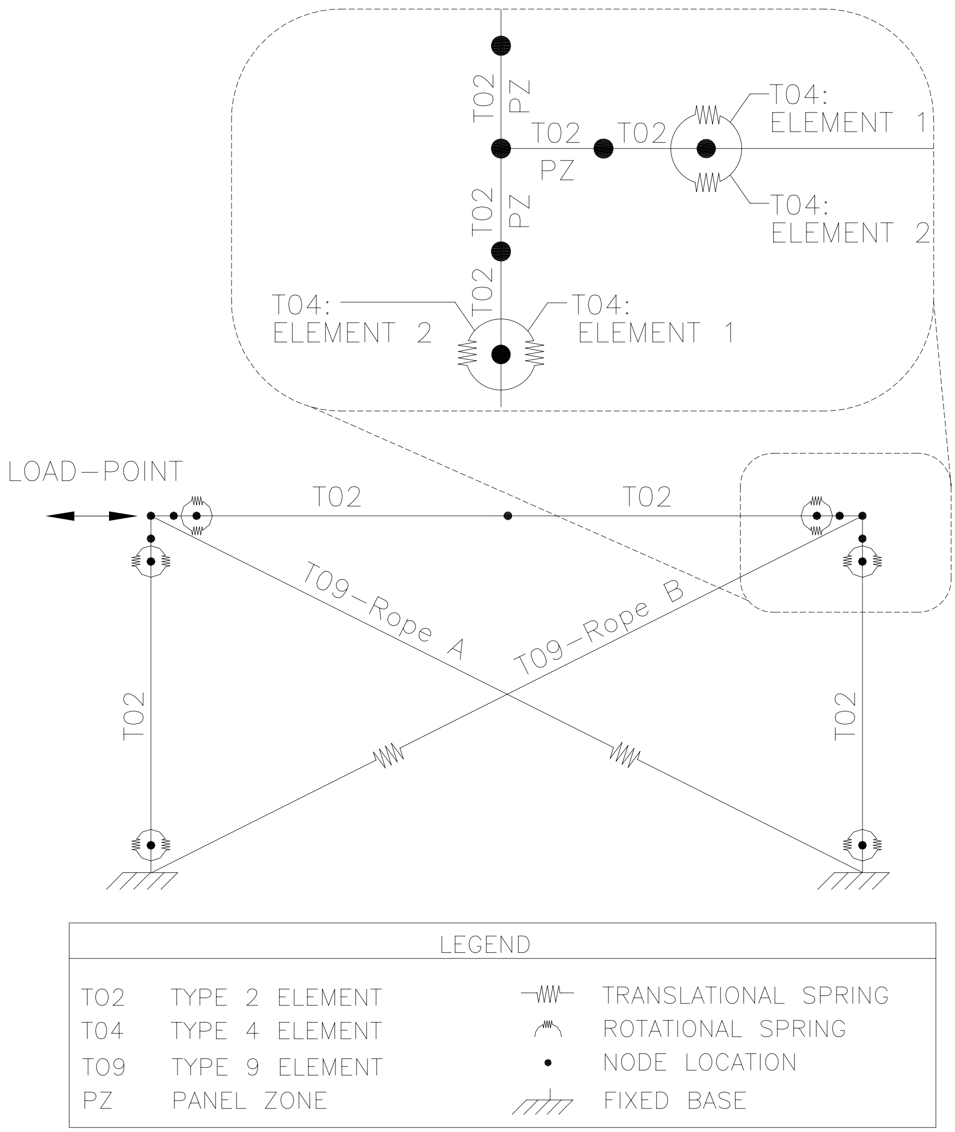

Figure D.2: 1:3-Scale Frame DRAIN Model

D.2 ANALYTICAL RESULTS

Comparisons of experimental versus DRAIN results for the 1:3-scale frame tests are shown in Figures D.3 through D.11. Load point displacement traces for tests conducted without ropes are shown in Figures D.3 through D.5. Load point displacement and rope force comparisons for tests conducted with ropes are shown in Figures D.6 through D.11.

Inelastic material behavior was observed for all tests conducted without ropes. Low level yielding in the column was observed for Tests 26 and Test 27. In Test 36, extreme levels of yielding were evident. Correlation between the experimental and analytical results was close, particularly for Test 26 and Test 28. Peak values for displacement found using DRAIN are within 5% of experimental values. Correlation of displacement data for Test 36 was less accurate, but acceptable. Peak analytical values for displacement are within 8% of experimental peak displacement.

For tests conducted with ropes, two levels of frame behavior were observed. In Test 27 the frame was observed to remain elastic, and a small amount of yielding was observed in Test 28. Variance in displacement correlation was within 10% between the analytical study and experimental results for both tests. Variance in correlation of peak rope force varies between 2% for Rope A, Test 27, to 10% for Rope B, Test 28.

Overall the correlation between the experimental and analytical results was acceptable. The model was therefore determined to be adequate for the purpose of predicting the inelastic response of a steel frame in which yielding occurs, and the response of the frame when ropes were added.

Two limitations of the model exist. First, initial stiffness of the frame was determined experimentally and matched by adjusting the panel zone stiffness values analytically. Without having accurate stiffness values at the beam to column connections, results would have been much less accurate. Secondly, it should be noted that forced loading was used for all tests. Therefore the accuracy of the analytical model in predicting frame and rope response due to inertial loading, including damping, remains unproven.

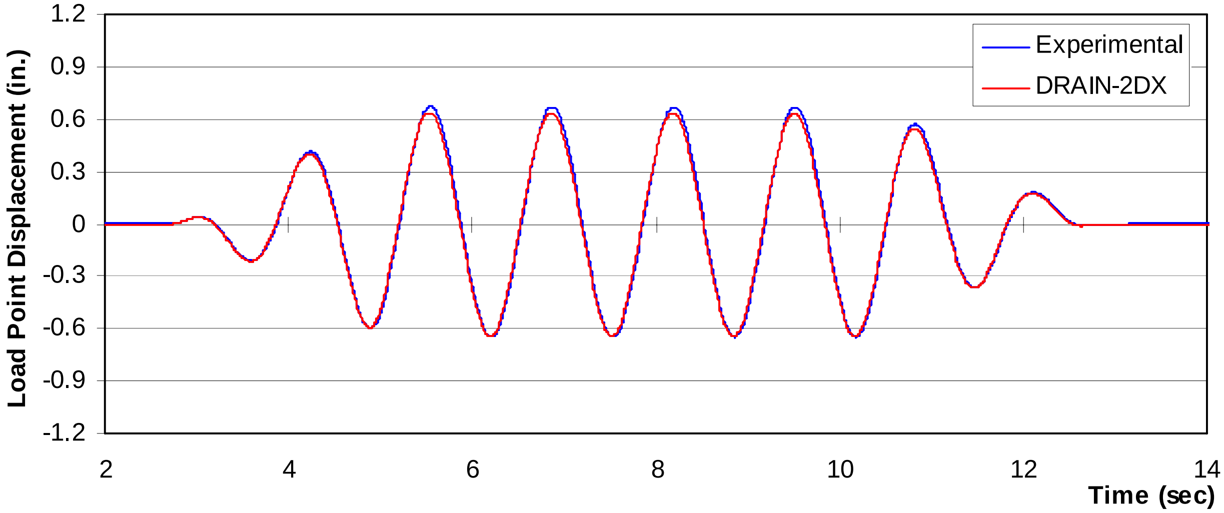

Figure D.3: Load Point Displacement Trace Comparison: Test 26

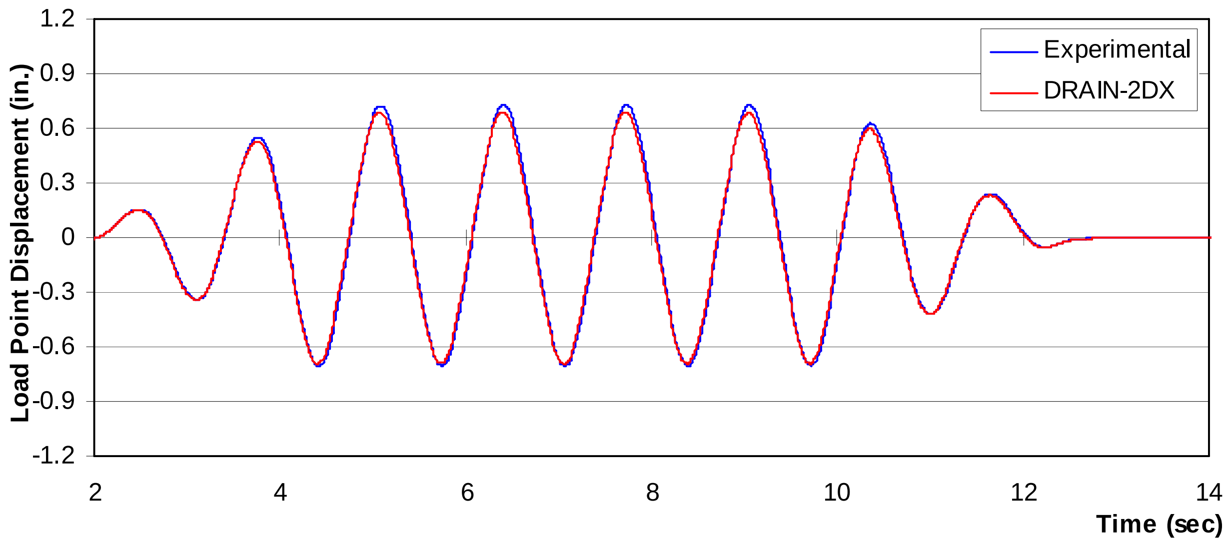

Figure D.4: Load Point Displacement Trace Comparison: Test 28

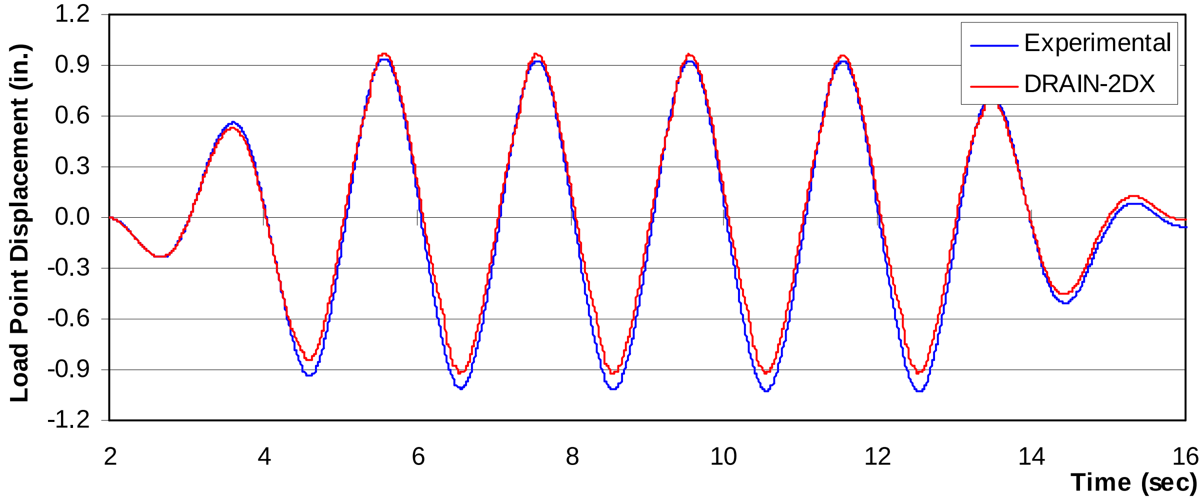

Figure D.5: Load Point Displacement Trace Comparison: Test 36

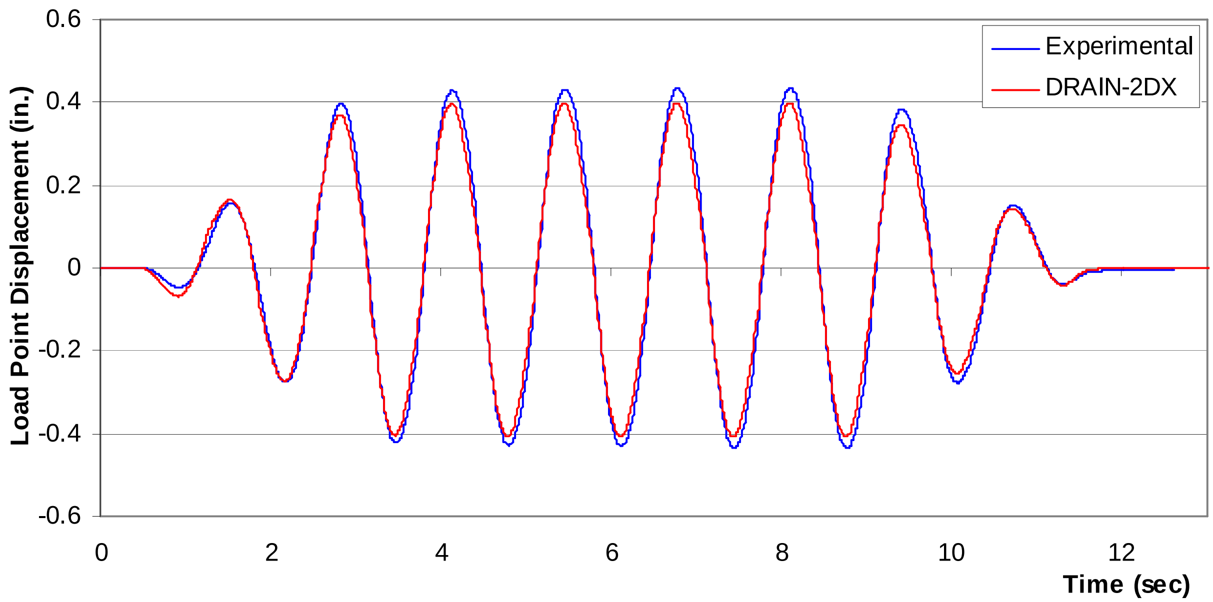

Figure D.6: Load Point Displacement Trace Comparison: Test 27

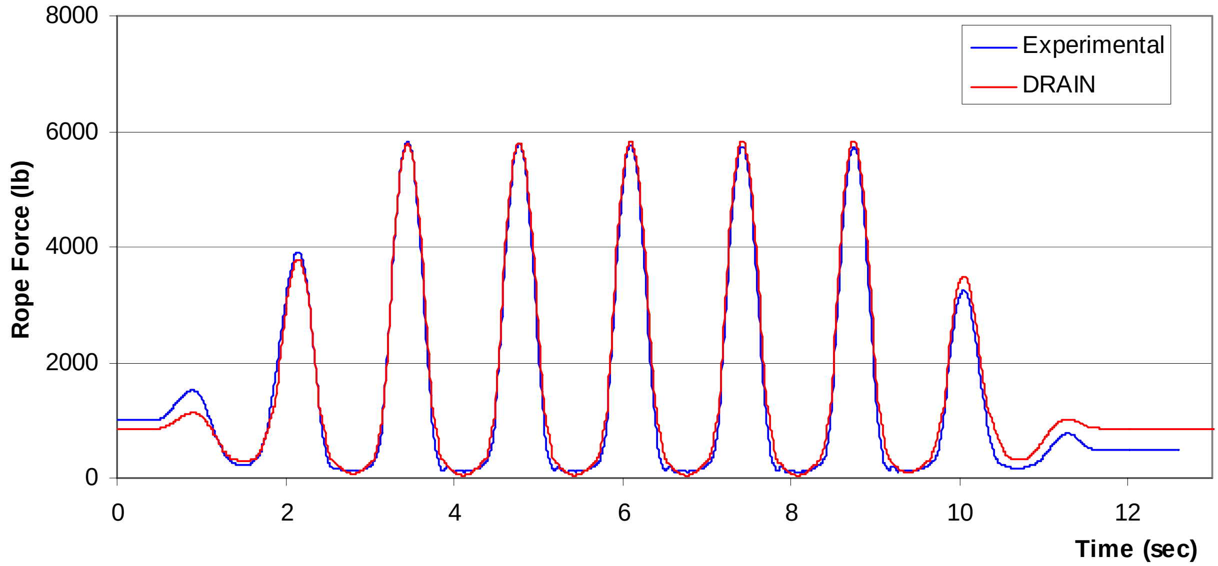

Figure D.7: Comparison of Force in Rope A: Test 27

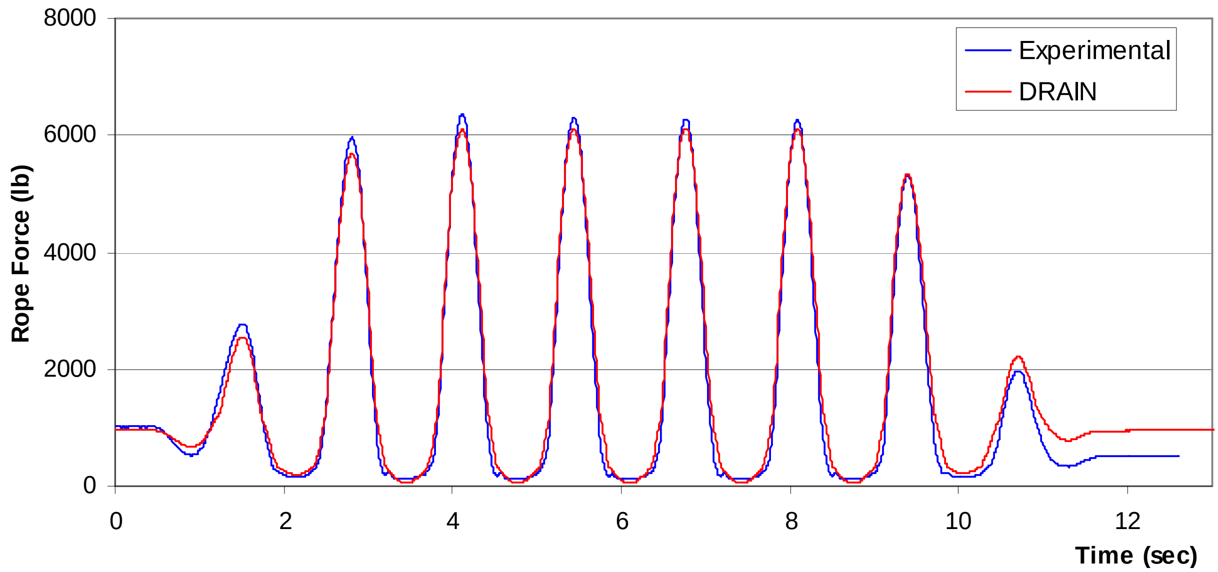

Figure D.8: Comparison of Force in Rope B: Test 27

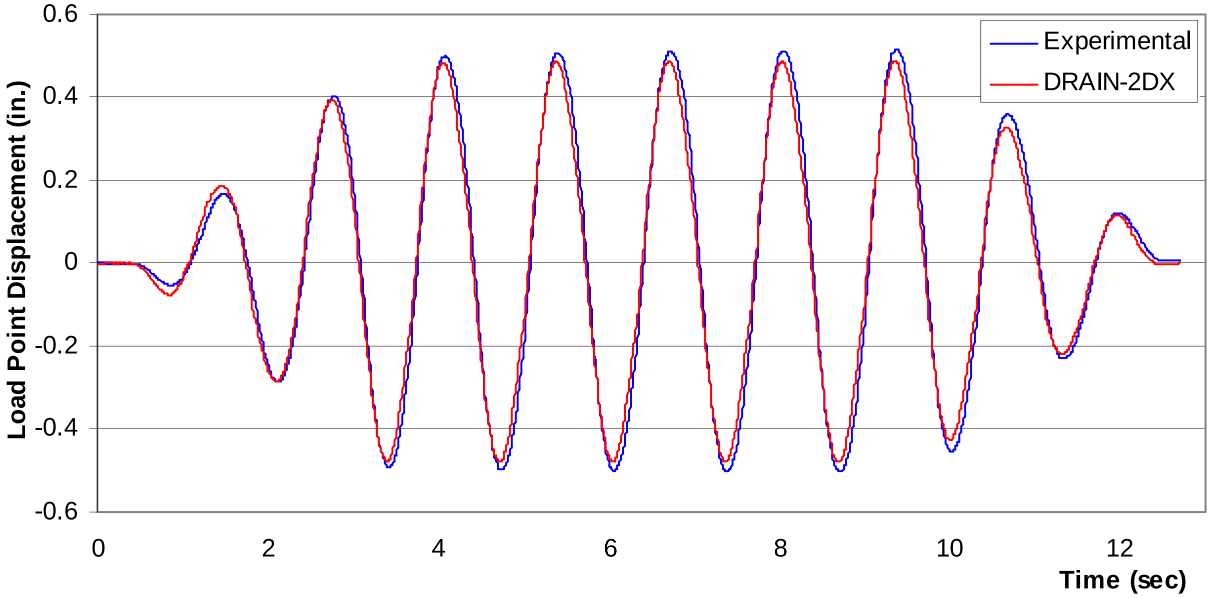

Figure D.9: Load Point Displacement Trace Comparison: Test 29

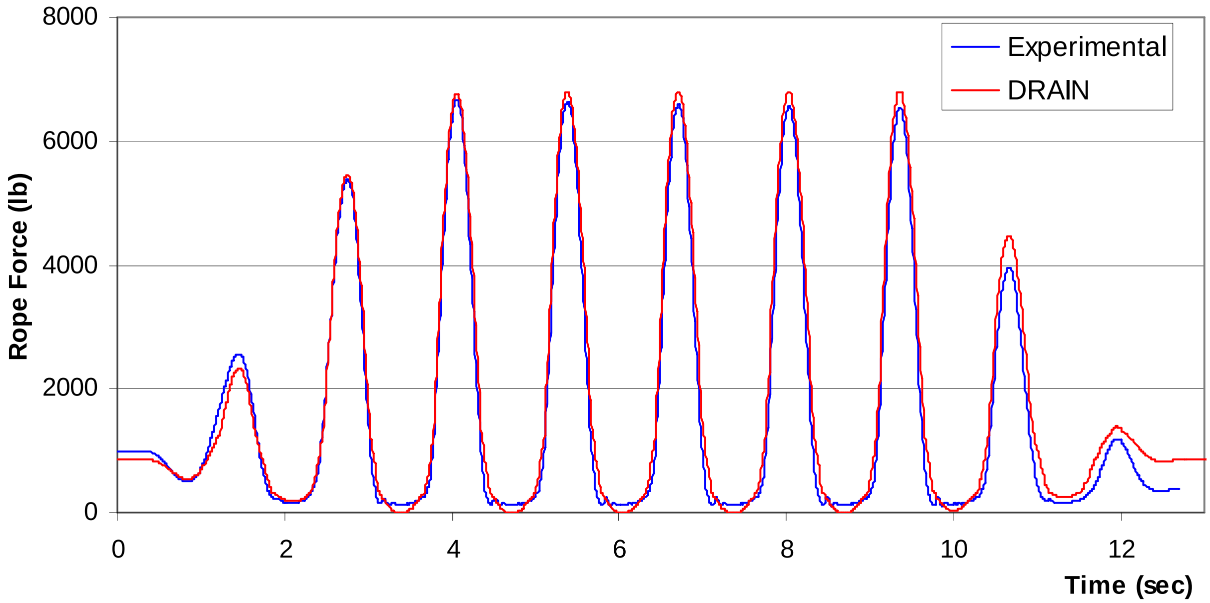

Figure D.10: Comparison of Force in Rope A: Test 29

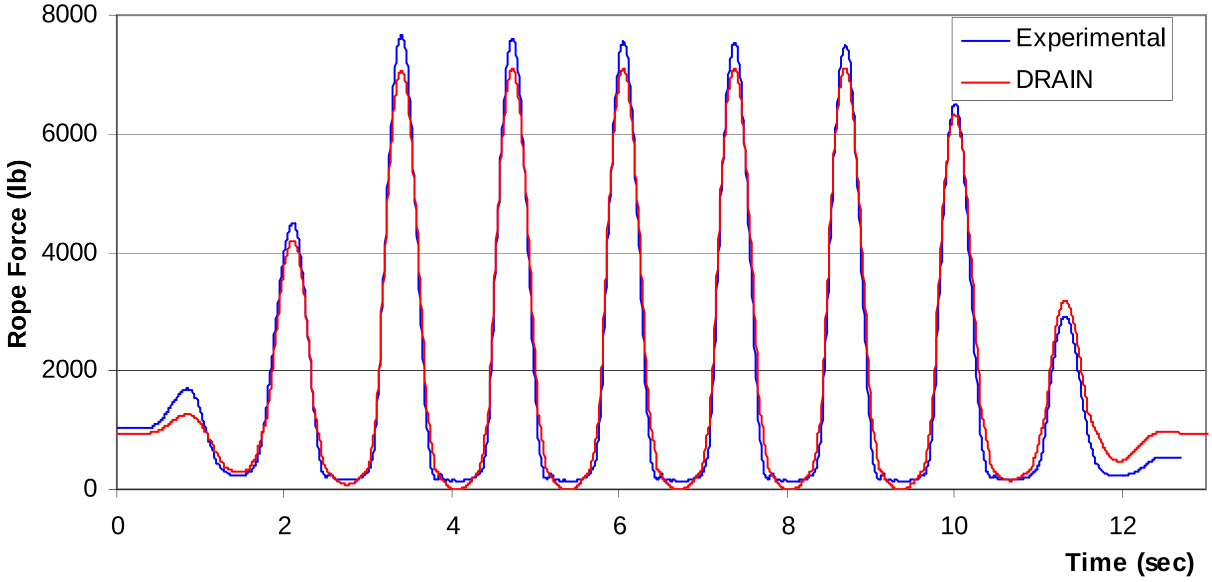

Figure D.11: Comparison of Force in Rope B: Test 29

APPENDIX E

1:6-Scale Frame Engineering Drawings

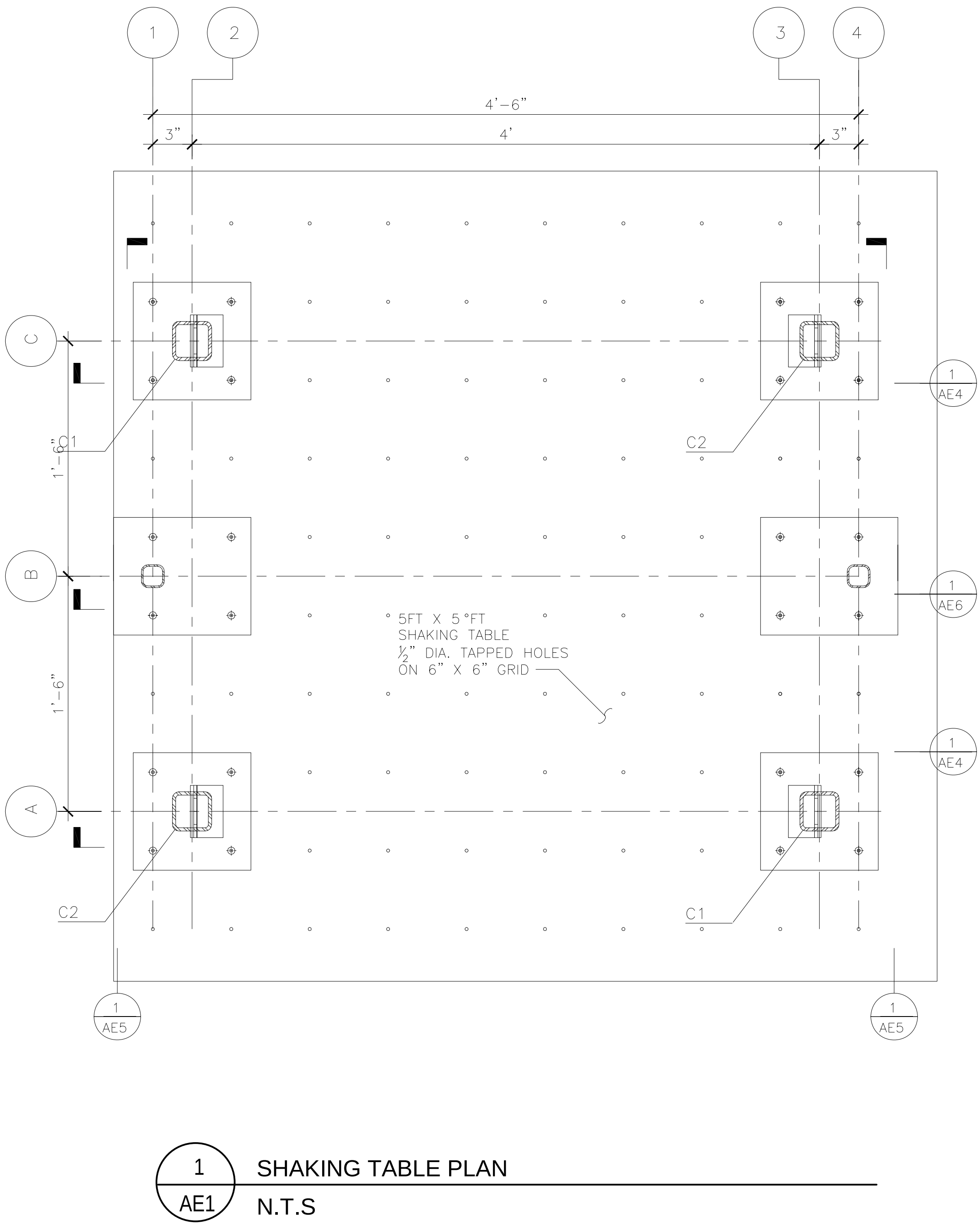

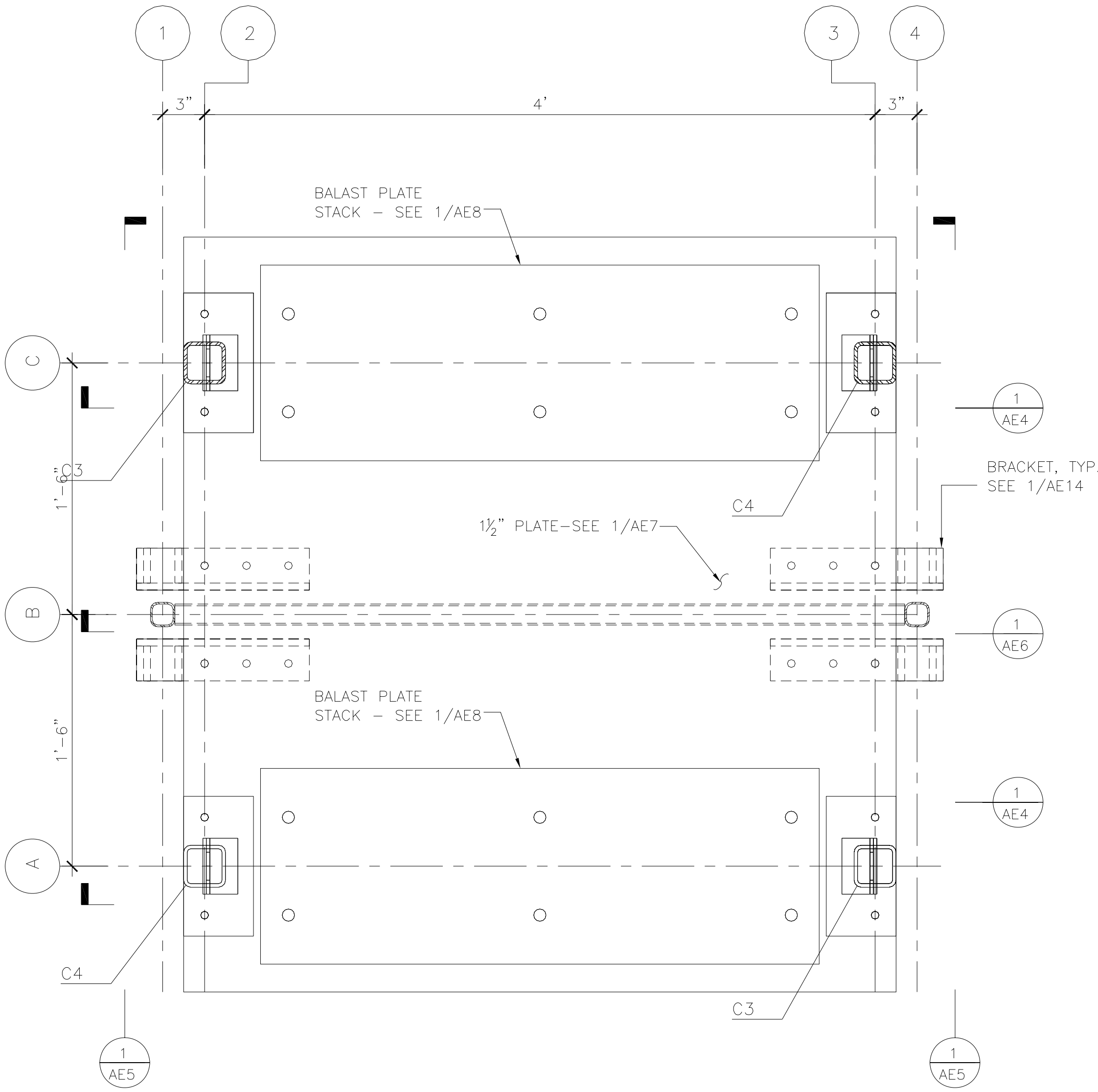

1 / AE2 SECOND FLOOR PLAN

N.T.S

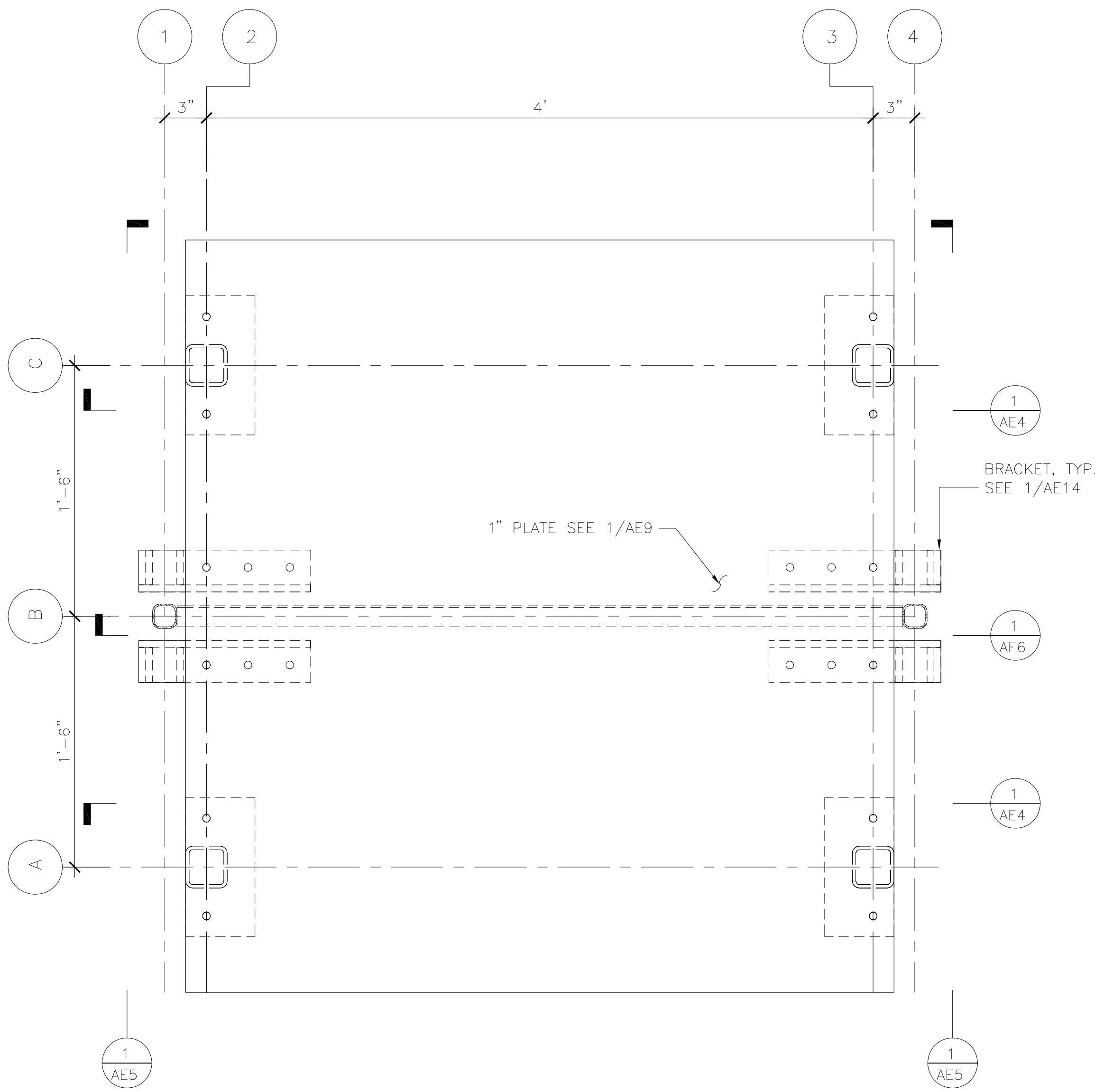

1 / AE3 ROOF PLAN

N.T.S

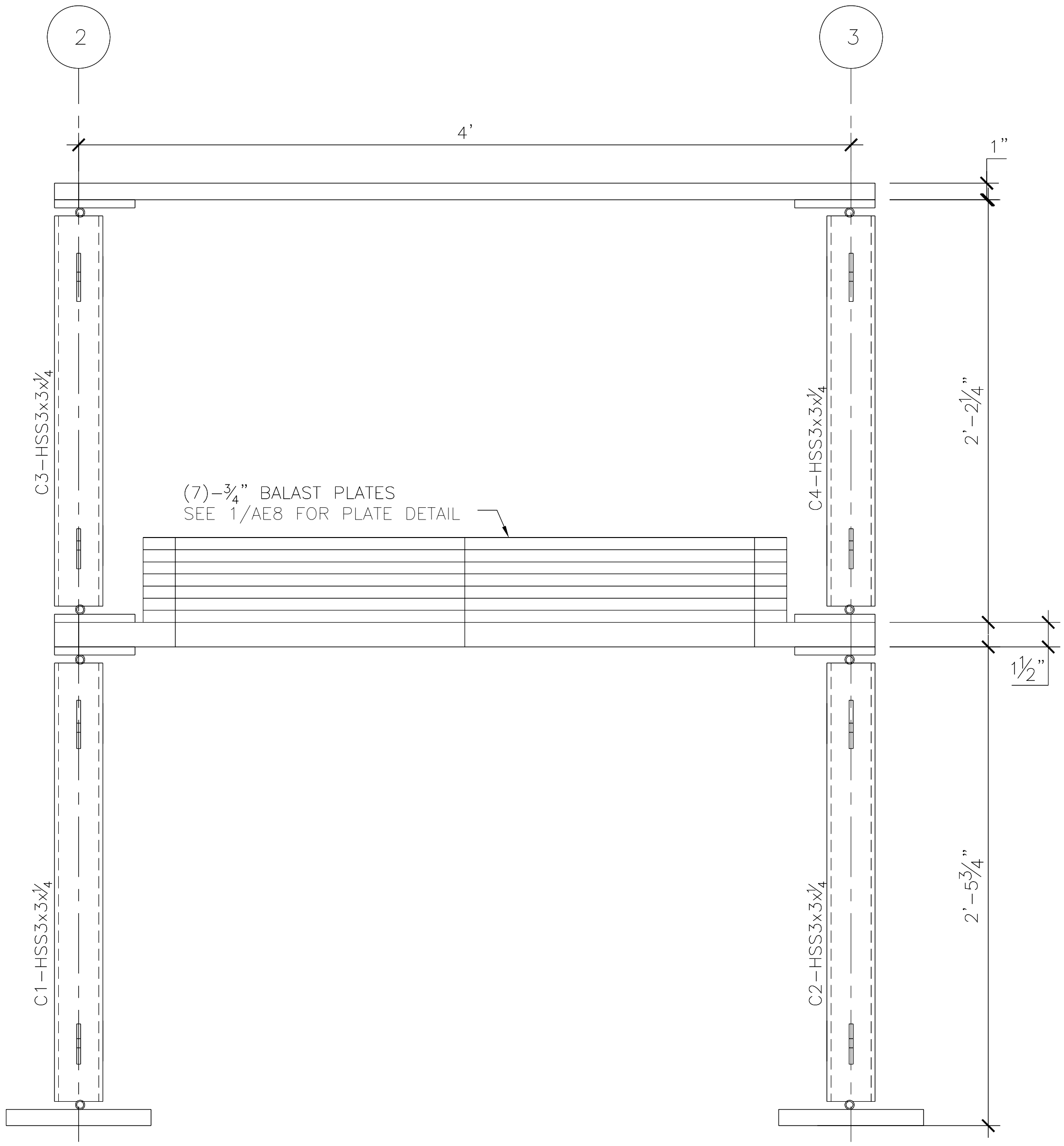

1
AE4

LEANER FRAME – SIDE ELEVATION

N.T.S

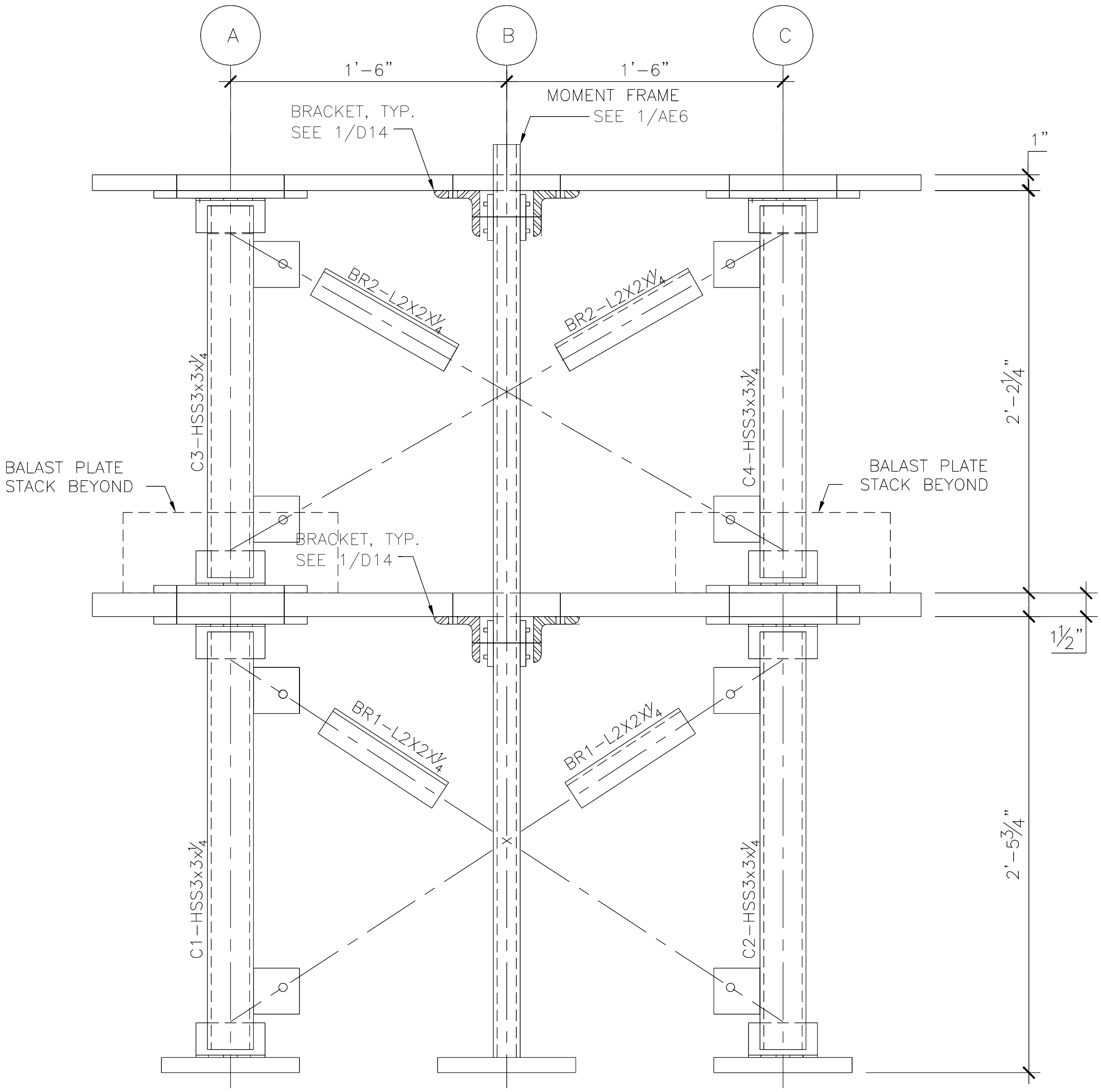

1 AE5 LEANER FRAME – END ELEVATION

N.T.S

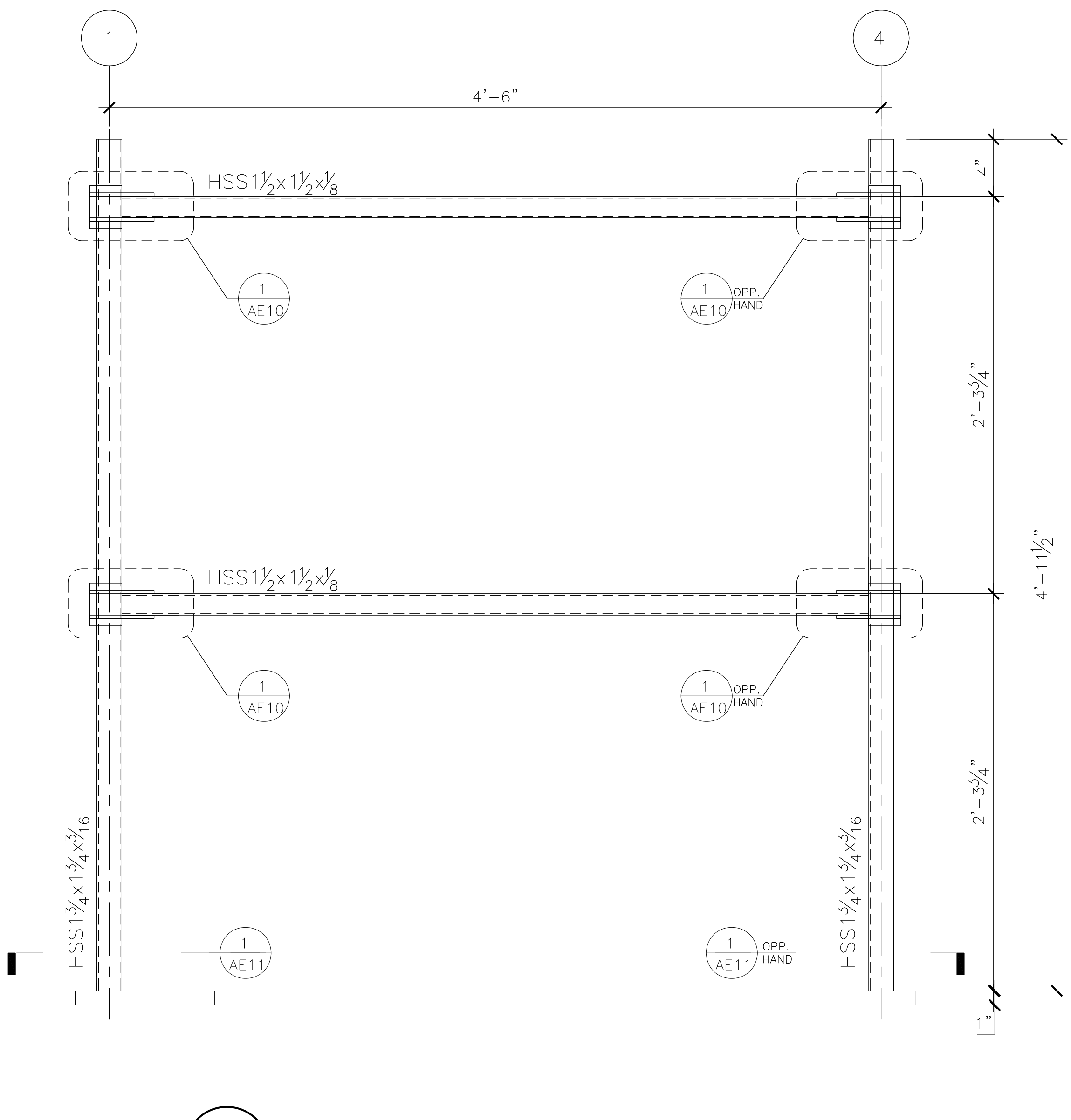

1
AE6
MOMENT FRAME ELEVATION
N.T.S

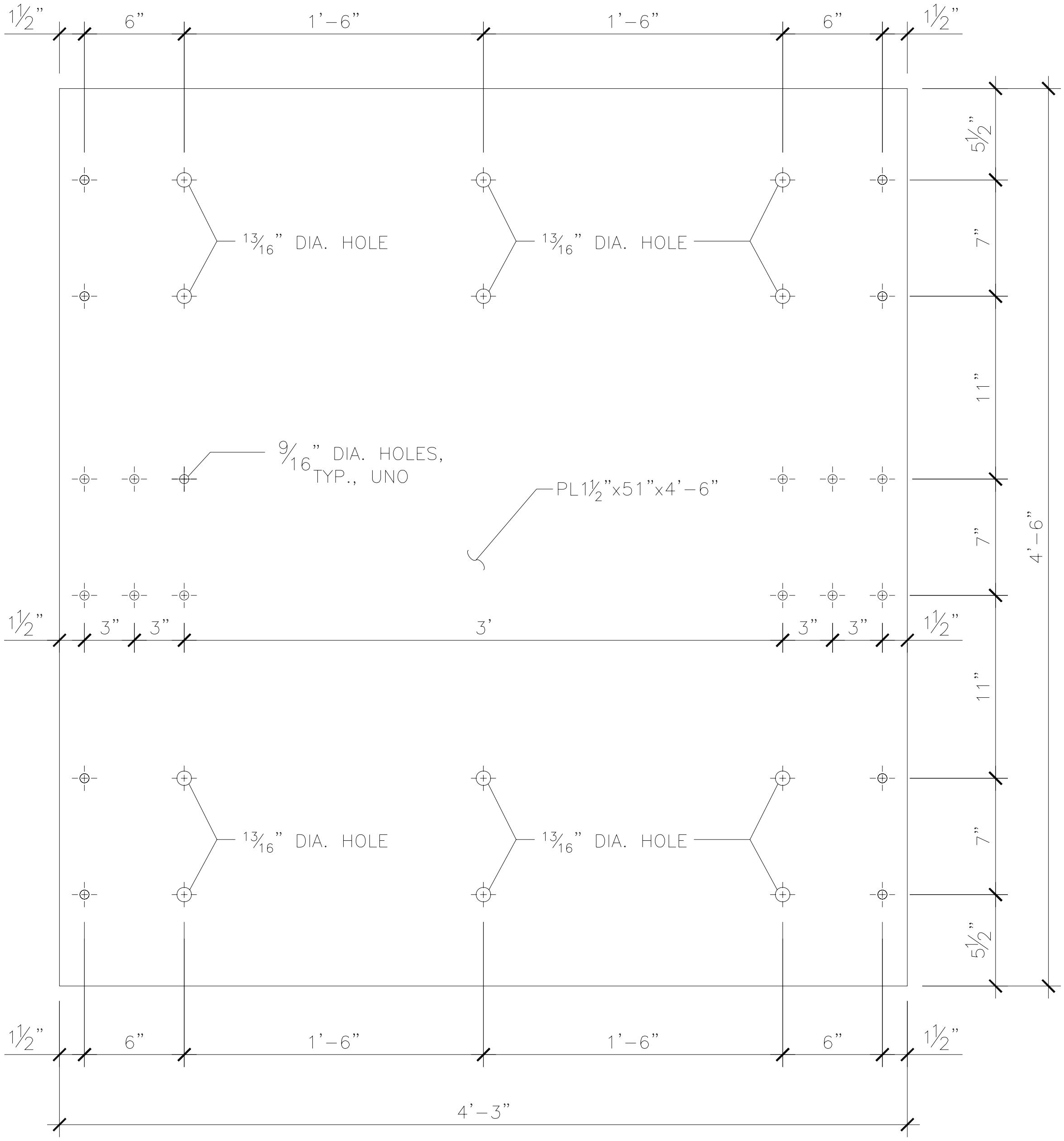

1
AE7

FLOOR DIAPRHAGM PLATE DETAIL

N.T.S

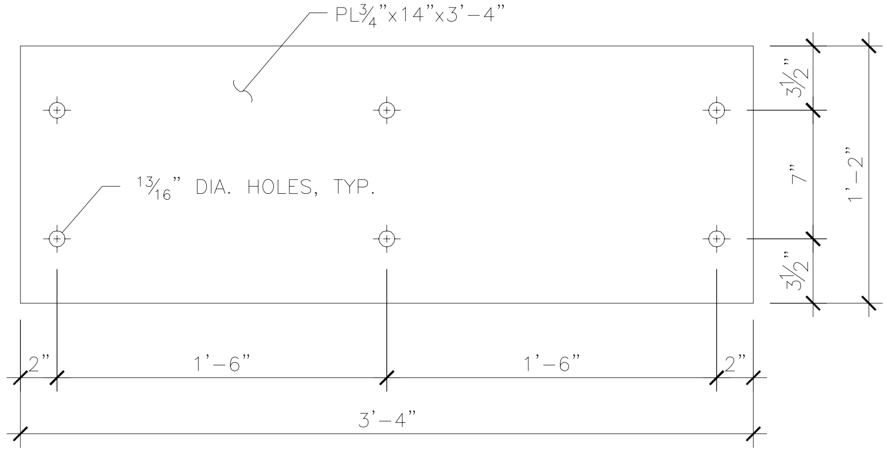

1
AE8

BALLAST PLATE DETAIL

N.T.S

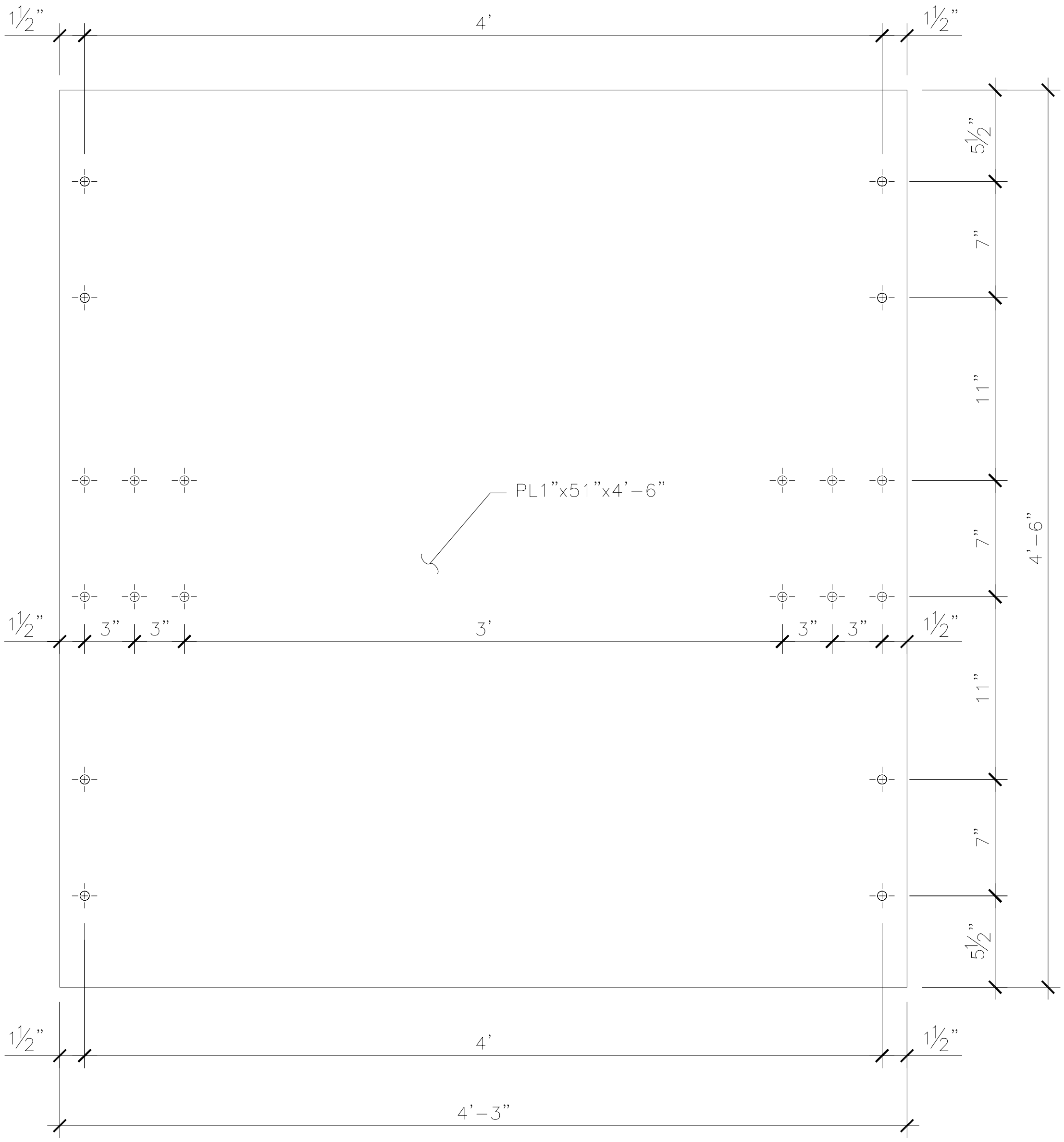

1
AE9

ROOF DIAPRHAGM PLATE DETAIL

N.T.S

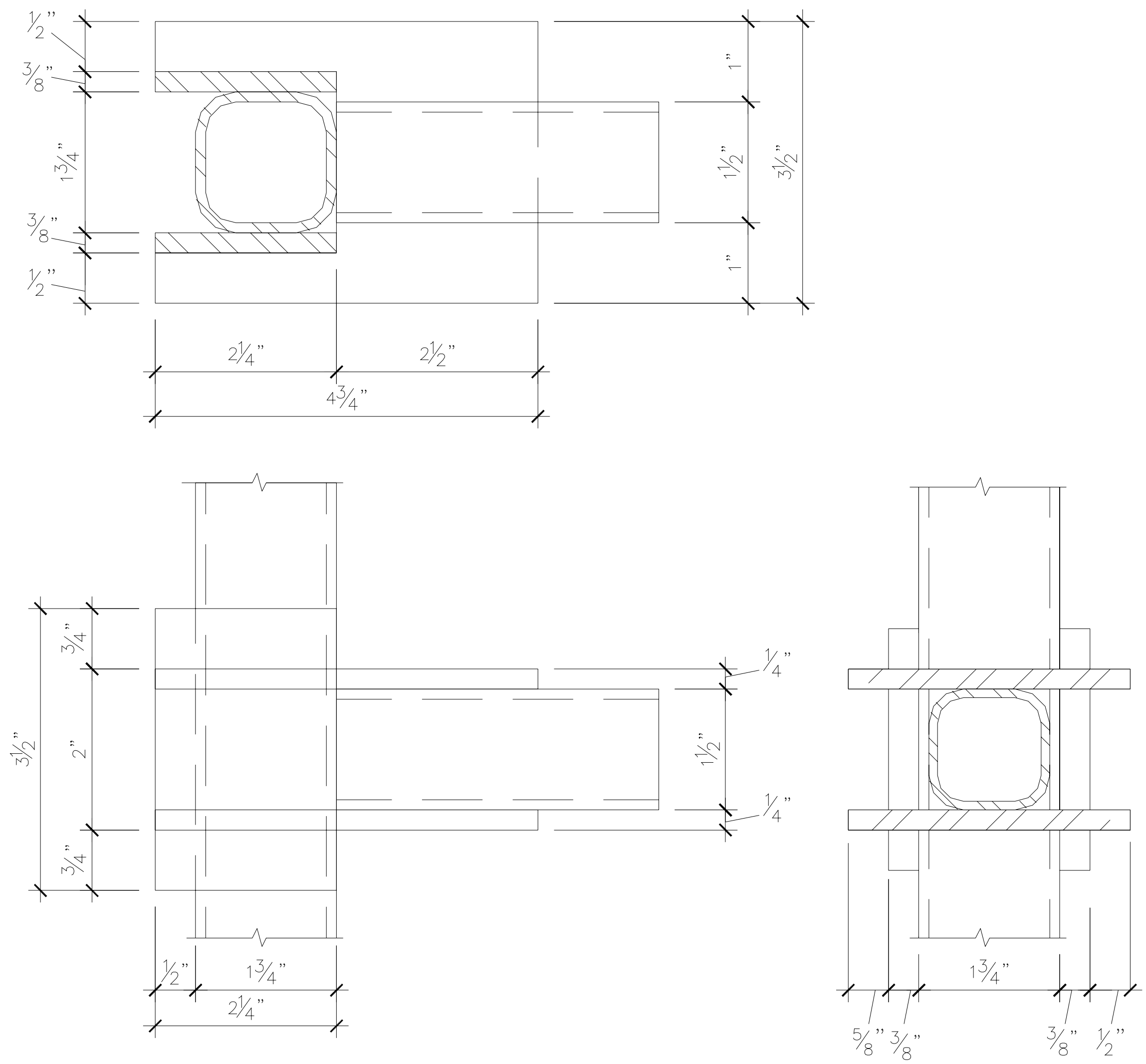

1
AE10

TYPICAL MOMENT CONNECTION DETAIL

N.T.S

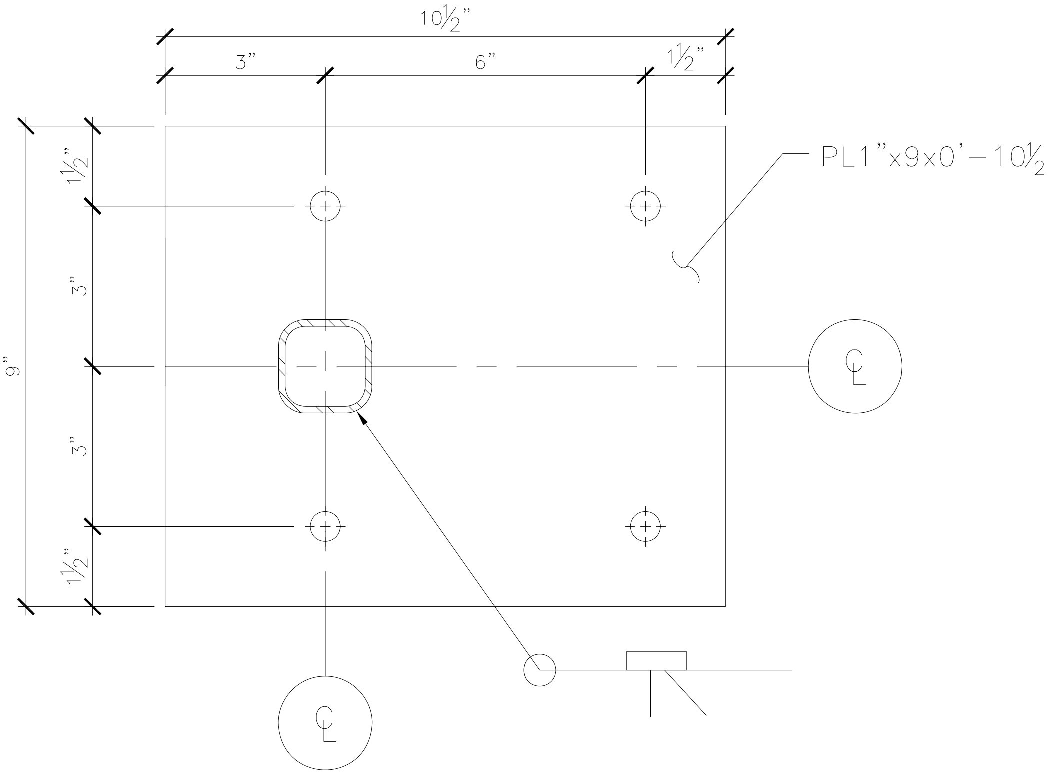

1 AE11 MOMENT FRAME BASE PLATE DETAIL
N.T.S

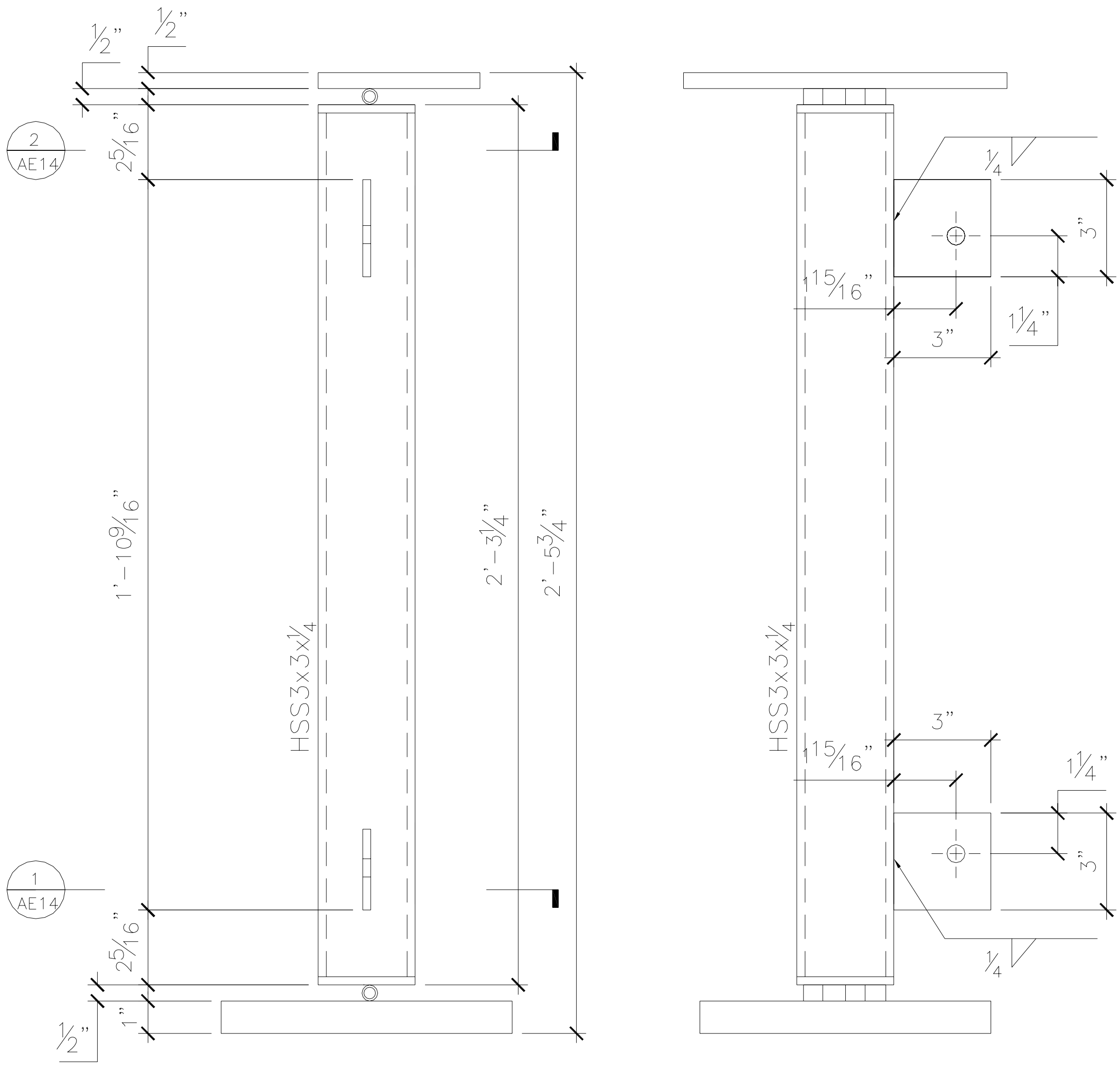

1 / AE12 LEANER-FRAME COLUMN (C1, C2-OPP. HAND)

N.T.S

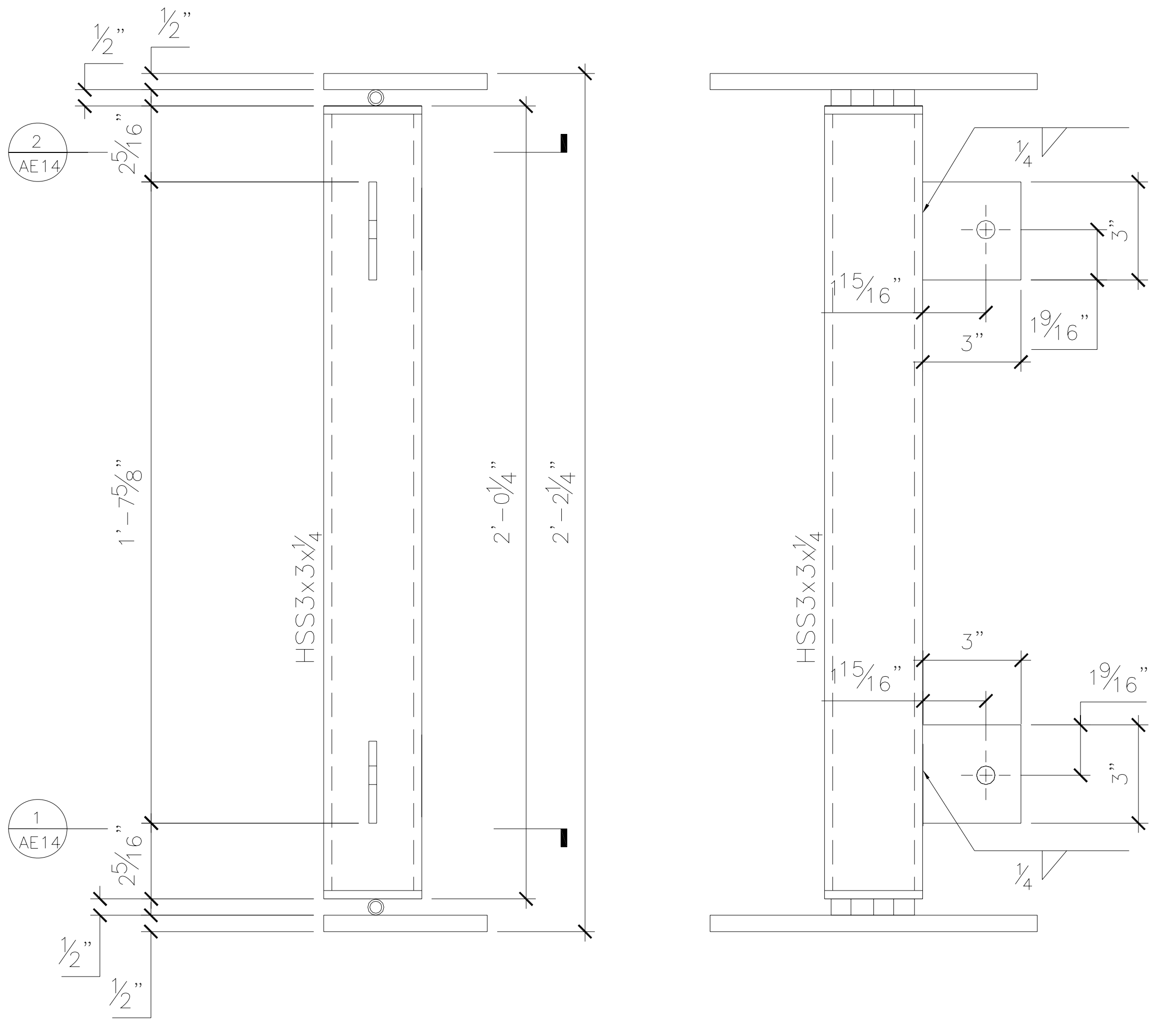

1
AE13

LEANER-FRAME COLUMN (C3, C4-OPP. HAND)

N.T.S

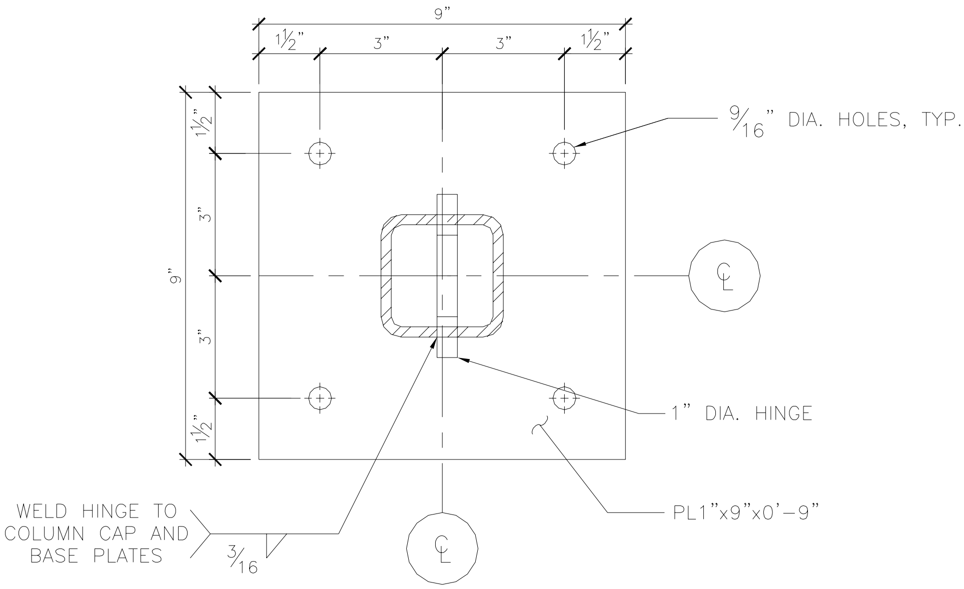

1 AE14 LEANER-FRAME BASE PLATE / HINGE

N.T.S

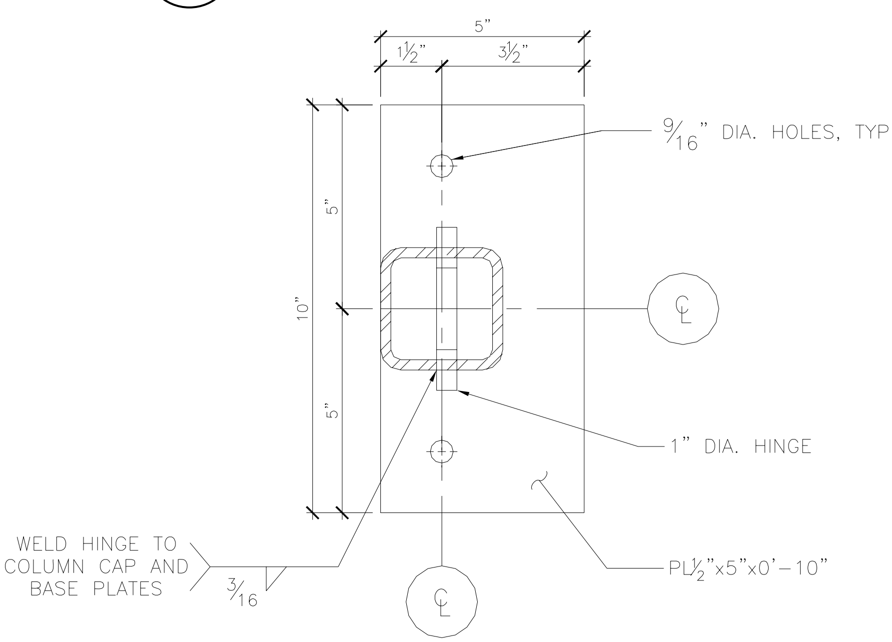

2 AE14 LEANER-FRAME BASE PLATE / HINGE

N.T.S

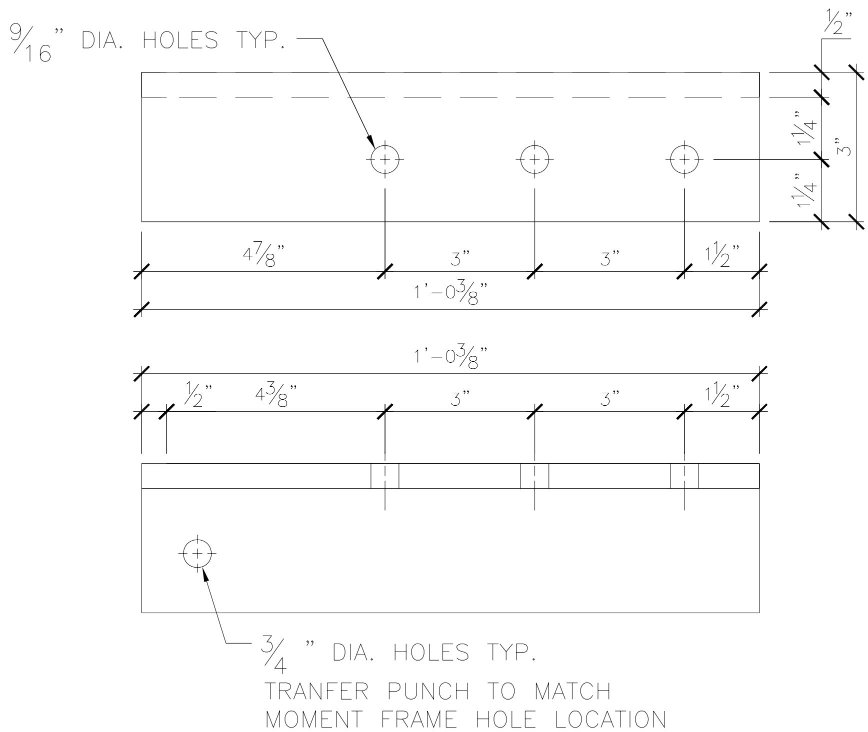

1
AE15

BRACKET DETAIL

N.T.S

Appendix F

Matlab Subroutine Used to Obtain Displacements from Experimental Acceleration Data

Author: H.P. Gavin, Dept. Civil and Environ. Eng'g, Duke Univ., Dec. 2005

```
function y = ftdsp(u,ni,flo,fhi,sr)
load NR180T1.mat
% y = ftdsp(u,ni,flo,fhi,sr)
% band-pass filter and integrate a discrete-time signal, u
%  u  : the discrete-time signal to be filtered/integrated, a column vector
% ni  : the number of integrations (may be zero or negative for differentiation)
% flo : the  low frequency limit for the bandpass filter  ( >= 0 )
% fhi : the high frequency limit for the bandpass filter  ( <= sr/2 );
% sr  : the sample rate

% H.P. Gavin, Dept. Civil and Environ. Eng'g, Duke Univ., Dec. 2005

 [N,C] = size(u);
 if N < C
   disp('ftdsp: u should be a column vector');
 end

% windowing the data can help with numerical accuracy
Nw = floor(N/10);       % number of window points
w = [ 0.5*(1-cos(pi*[0:Nw]/Nw)) ones(1,N-2*Nw-2) 0.5*(1+cos(pi*[0:Nw]/Nw)) ]';
u = u .* w;         % comment out this line for no windowing

 NF = 2 ^ ceil( log(N)/log(2) );    % use 2^n points for FFT calculations

 delta_f = sr/NF;          % frequency resolution

 f = [ [0:NF/2] [-NF/2+1:-1] ]' * delta_f;  % frequency data


 kloP = max(floor( flo/delta_f) + 1, 1 );
 khiP = min(floor( fhi/delta_f) + 1, NF/2+1 );
 kloN = min( ceil(-flo/delta_f) + 1 + NF, NF );
 khiN = max( ceil(-fhi/delta_f) + 1 + NF, NF/2+2 );

 H = zeros(NF,1);          % initialize filter transfer function

 H([kloP:khiP]) = 1;           % positive band pass frequencies
```

```
H([khiN:kloN]) = 1;          % negative band pass frequencies

if ( kloP > 2 )       % smooth the  low-frequency transition band
    disp(kloP+1);
  H([ kloP+1 kloN-1 ]) = 3/4;
  H([ kloP   kloN   ]) = 1/2;
  H([ kloP-1 kloN+1 ]) = 1/4;
end
if ( khiP < NF/2+1 )      % smooth the high-frequency transition band
  H([ khiP-1 khiN+1 ]) = 3/4;
  H([ khiP   khiN   ]) = 1/2;
  H([ khiP+1 khiN-1 ]) = 1/4;
end

i  = sqrt(-1.0);          % the imaginary number

ID = (i*2*pi*f).^(-ni);  ID(1) = 1;    % integration/differentiation filter


U  = fft(detrend(u),NF);   % take the FFT of the real signal, u


Y  = [ H.*ID*ones(1,C) ].*U;   % convolution with the filter transfer function

y  = ifft(Y,NF);      % Inverse FFT

if ( ( max(norm(imag(y)') ./ norm(real(y)')) ) > 1e-4 )
   disp( norm(imag(y)') ./ norm(real(y)') )
   disp('ftdsp: uh-oh, the imaginary part should be practically zero');
end

y = real(y(1:N,:));       % retain only the original N data points
```

REFERENCES

ACI (2005). *Building Code Requirements for Structural Concrete (ACI318-02)*. American Concrete Institute, Farmington Hills, MI.

Aguirre, M. and Sanchez, A.R. (1992). "Structural Seismic Damper." *Journal of Structural Engineering*, Vol. 118, pp. 1158-1172.

Aguirre, M. and Aguirre, R. (2000). "Antiseismic Structure: Damper-Equipped Elastic Frame." *Proceedings of the Institution of Civil Engineering Structures and Buildings*, Vol. 146, pp. 147-159.

AISC (2005a). *Specifications for Structural Steel Buildings.* American Institute of Steel Construction, Chicago, IL.

AISC (2005b). *Seismic Provisions for Structural Steel Buildings.*, American Institute of Steel Construction, Chicago, IL.

AISC (2002). *Seismic Provisions for Structural Steel Buildings*. American Institute of Steel Construction, Chicago, IL.

Batt, D.P. and Gavin, H.P. (1999). "Testing of a Scaled Seismically-Isolated Structure Using a Hydraulic Shaking Table". National Science Foundation Reports CMS-9622177 and CMS-9624949, Department of Civil and Environmental Engineering, Duke University, Durham, NC.

Black, J., Makris, N., and Aiken, I.D. (2004). "Component Testing, Seismic Evaluation and Characterization of Buckling-Restrained Braces." *Journal of Structural Engineering*, Vol. 130, pp. 880-894.

Chang, K. C., Soong, T.T., Oh, S.-T., and Lai, M.L. (1992). "Ambient Temperature on a Viscoelastically Damped Structure." *Journal of Structural Engineering,* Vol. 118, pp. 1955-1973.

Chang, K. (1995). "Seismic Behavior of Steel Frame with Added Viscoelastic Dampers." *Journal of Structural Engineering*, Vol.121, pp.1418-1426.

Constantinou, M.C. and Symans, M.D. (1992). "Experimental and Analytical Investigation of Seismic Response of Structures with Supplemental Fluid Viscous Dampers." National Center For Earthquake Engineering (NCEER) Technical Report 92-0032, Buffalo, NY.

Constantinou, M.C., Soong, T.T., and Dargush, G.F. (1998). "Passive Energy Dissipation Systems for Structural Design and Retrofit." Multidisciplinary Center for Earthquake Engineering Research (MCEER) Monograph No. 1, Buffalo, NY.

Corbi, O. (2003). "Shape Memory Alloys and Their Application in Structural Oscillations Attenuation." *Simulation Modelling Practice and Theory*, Vol. 11, pp. 387-402.

EERI (2003), *Securing Society Against Catastrophic Earthquake Loss: A Research and Outreach Plan in Earthquake Engineering, Draft Report*, Earthquake Engineering Research Institute, Oakland CA.

FEMA (2000a), “Recommended Seismic Design Criteria for New Steel Moment-Frame Buildings.” Federal Emergency Management Agency Report No. 350.

FEMA (2000b). “Commentary on Recommended Seismic Design Criteria for New Steel Moment-Frame Buildings.” Federal Emergency Management Agency Report No. 352.

FEMA (2000c). “Recommended Post-earthquake Evaluation and Repair Criteria for Welded Steel Moment Frames.” Federal Emergency Management Agency Report No. 352.

FEMA (2000d). “Pre-Standard and Commentary for the Seismic Rehabilitation of Buildings.” Federal Emergency Management Agency Report No. 356.

FEMA (2003a). “NEHRP Recommended Provisions for Seismic Regulations for New Buildings and Other Structures.” Federal Emergency Management Agency Report No. 450-1.

FEMA (2003b), “Commentary to the NEHRP Recommended Provisions for Seismic Regulations for New Buildings and Other Structures.” Federal Emergency Management Agency Report No. 450-2.

Filiatrault, A., Tremblay, R., and Kar, R. (2000). “Performance Evaluation of Friction Spring Seismic Dampers.” *Journal of Structural Engineering*, Vol. 4, pp. 491-499.

Flory, J.F., Mercer, D.E. (1997). “The New Cordage Institute Fiber Ropes Testing Methods.” *Oceans ’97*, IEEE, Poises, NJ.

Gavin (2003). *CE281 Course Notes: Scale Modeling and the Buckingham-PI Theorum*. Duke University, Duhram, N.C.

Guo, A.X., Xu, Y.L., and Wu, B. (2002). “Seismic Reliability Analysis of Hysteretic Structure with Viscoelastic Dampers.” *Engineering Structures*, Vol. 24, pp. 373-383.

Hennessey, C.M. (2003) “Analysis and Modeling of Snap Loads on Synthetic Fiber Ropes”. M.S. Thesis, Virginia Polytechnic Institute and State University, Blacksburg, VA.

Hooker, J. (2000). “Latest Synthetic Fiber Rope Developments in the Towage Industry.” International Tug and Salvage Convention, New Jersey.

Huang, X. and Vinogradov, O.G. (1996). “Dry Friction Losses in Axially Loaded Cables.” *Structural Engineering and Mechanics*, Vol. 4, pp. 330-344.

Ibrahim, Y. and Charney, F.A. (2006). “Analysis of Elasto-Plastic Dampers”, currently under review for publication in Journal of Constructional Steel Research.

Kikites, A., Lam, T.C., Mansour, N., and Nabavi, A. (2004). “A Study on the Use of Friction Dampers for the Seismic Upgrade of Structures.” (http://www.civ.utoronto.ca/profs/christopoulos/group_2.pdf)

Labrosse, M., Nawrocki, A., and Conway, T. (2000). “Frictional Dissipation in Axially Loaded Simple Straight Strands.” *Journal of Engineering Mechanics*, Vol. 126, pp.641-646.

Lai, M.L., Chang K.C., Soong, T.T., Hao, D.S., Yeh, Y.C. (1995). "Full-scale Viscoelastically Damped Steel Frame." Journal of Structural Engineering, Vol. 121, 1995, pp.1443-1447.

Lee, D.G., Hong, S., and Kim, J. (2002). “Efficient Seismic Analysis of Building Structures with Added Viscoelastic Dampers.” *Engineering Structures*, Vol. 24, pp. 1217-1227.

Leech, C.M. (2002). “The Modeling of Friction in Polymer Fiber Ropes.” *International Journal of Mechanical Sciences*, Vol. 44, pp. 621-643.

Levy, R., Marianchik, E., Rutenberg, A., and Segal, F. (2001). “A Simple Approach to the Seismic Design of Friction Damped Braced Medium-Rise Frames.” *Engineering Structures*, Vol. 23, pp. 250-259.

Miyamoto, K. and Hanson, R.D. (2002). “U.S. Design of Structures with Damping Systems.” Taylor Devices Publication, Taylor Devices Inc., North Tonawanda, NY.

Mualla, I.H. and Belev, B. (2002). “Performance of Steel Frames with a New Friction Damper Device Under Earthquake Excitation.” *Engineering Structures*, Vol. 24, pp. 365-372.

Nonlin-Pro (2003). Advanced Structural Concepts, Inc., Blacksburg, VA.

Pearson, N.J. (2002) “Experimental Snap Loading of Synthetic Fiber Ropes”. M.S. Thesis, Virginia Polytechnic Institute and State University, Blacksburg, VA.

Peckan, G., Mander, J. B., and Chen, S. S. (2000a). “Experiments on Steel MRF Building with Supplemental Tendon System.” *Journal of Structural Engineering*, Vol. 126, pp. 437-444.

Peckan, G., Mander, J. B., and Chen, S. S. (2000b). “Balancing Lateral Loads Using Tendon-Based Supplemental Damping System.” *Journal of Structural Engineering*, Vol. 126, pp. 896-905.

Phocas, M.C. and Pocanschi, A. (2003). “Steel Frames with Bracing Mechanism and Hysteretic Dampers.” *Earthquake Engineering and Structural Dynamics*, Vol. 32, pp. 811-825.

Prakish, V., Powell, G.H., and Cambell, S. (1993). “DRAIN-2DX: Base Program Description and User Guide”, RAM International, Carlsbad, CA.

RISA (2004). “RISA-3D (Version 6)”, RISA Technologies, Foothill Ranch, CA.

Ringleb, F.O. (1957). “Motion and Stress of an Elastic Cable Due to Impact.” *Journal of Applied Mechanics*, Vol. 24, pp. 417-425.

Sauter, D. and Hagedorn, P. (2002). “On the Hysteresis of Wire Cables in Stockbridge Dampers.” *International Journal of Non-Linear Mechanics*, Vol. 37, pp. 1453-1459.

Shen, K.L., Soong, T.T., Chang, K.C., and Lai, M.C. (1995). “Seismic Behavior of Reinforced Concrete Frames with Added Viso-Elastic Dampers.” *Engineering Structures*. Vol. 9, pp. 141-296.

Shukla, A.K. and Datta, T.K. (2001). “Analysis of Building Frames with Viscoelastic Dampers Under Base Excitation.” *Structural Engineering and Mechanics*, Vol. 2, pp. 71-87.

Sauter, D. and Hagedorn, P. (2001). “On the hysteresis of Wire Cables in Stockbridge Dampers,” International Journal of Non-Linear Mechanics, Vol. 37, pp. 1453-1459.

Talwani, P. and Schaeffer, W.T. (2001). “Recurrence Rates of Large Earthquakes in the South Carolina Coastal Plain Based on Paleoliquefaction Data”, *Journal of Geophysical Research-Solid Earth*, Vol. 106, pp. 6621-6642.

Taylor, D.P. (2001). “Viscous Damper Development and Trends.” *Structural Design of Tall Buildings*, Vol. 10, pp. 311-320.

Wallace, B.J. and Krawinkler, H. (1999). “Small-Scale Model Tests of Steel Assemblies,” *Journal of Structural Engineering*, Vol. 115, pp. 1999-2015.

Wu, Huai-Chung, Seo, M.H., and Backer, S. (1995). “Structural Modeling of Double Braided Synthetic Fiber Ropes.” *Textile Research Journal*, Vol. 65, pp.619-632.

Xia, C. and Hanson, R.D. (1994). “Influence of ADAS Element Parameters on Building Seismic Response.” *Journal of Structural Engineering*, Vol. 118, pp. 1903-1918.

VITA

John C. Ryan, Jr. was born in Slidell, Louisiana on February 19, 1975. After graduating from Slidell High School in 1993, he began work on a Bachelor of Science degree in Civil Engineering at Louisiana State University in Baton Rouge, Louisiana. In the fall of 1996, he began an exchange program at Virginia Tech in Blacksburg, Virginia for one semester. The exchange was extended to two semesters, at which time John transferred to Virginia Tech, where he completed a Bachelor of Science degree in Civil Engineering in May, 1998. He immediately began work on a Master of Science degree in Civil Engineering, which was completed in September, 1999. John accepted a position as a structural design engineer with Starzer, Brady, Fagan Associates, Inc., located in Atlanta, Georgia, in December, 1999. John married Amy Janel Dalrymple on April 6, 2002. After being accepted into the Doctoral Program in the Civil Engineering Department at Virginia Tech, John moved back to Blacksburg and entered the program in August, 2003. John completed the requirements for a Ph.D. in Civil Engineering during Fall, 2006. John will begin working for StructurTech Construction Systems in Charleston, South Carolina in October, 2006.